JOINT EUROPEAN TORUS

JET–P(90)73

A. Bondeson, R. Parker, M. Hugon
and JET Team

MHD Modelling of Density Limit Disruptions in Tokamaks Final Report of Article 14 Contract JWS/9007

MHD Modelling of Density Limit Disruptions in Tokamaks Final Report of Article 14 Contract JWS/9007

A. Bondeson[1], R. Parker[1], M. Hugon
and JET Team*

JET-Joint Undertaking, Culham Science Centre, OX14 3DB, Abingdon, UK

[1]Centre de Recherches en Physique des Plasmas, Association Euratom-Confederation Suisse, Ecole Polytechnique Federale de Lausanne, Lausanne, Switzerland
** See Appendix 1*

Preprint of Paper to be submitted for publication in
Nuclear Fusion

ABSTRACT.

The magnetohydrodynamic (MHD) activity during density limit disruptions is modeled numerically by three-dimensional resistive reduced MHD simulations with a simple transport model and radiation losses. The simulations reproduce experimentally observed phenomena such as the destabilization of MHD modes near the plasma edge during the early profile contraction phase, followed by growth of the m=2/n=1 mode to large amplitude, a sequence of minor disruptions and the major disruption. A new theoretical model is given for the major disruption, which takes place in two phases: first, an internal relaxation flattens the temperature in the central part and subsequently, the current profile broadens. The internal instability of the first phase has a mainly m=1/n=l displacement, but because of nonlinear coupling to the large m=2/n=1 mode, the magnetic perturbation has a strong m=3/n=2 component. At a late stage of the internal relaxation, the large amplitude 2/1, 1/1, and 3/2 perturbations give rise to stochastic magnetic fields in the q=l island, and at its end, the magnetic field is stochastic in the region $q \leq 2$. During the second phase, MHD turbulence develops on the stochasticized fields, resulting in filamentation and broadening of the current density, first in the central region. The disruption ends with a rapid instability of the $m \geq 2/n=1$ modes. The result is stochastic magnetic fields across the entire plasma and a large-scale broadening of the current profile.

1. INTRODUCTION

The phenomenon of major disruption in tokamaks is well known experimentally [1-9]. It is of considerable importance for several reasons. First, the onset of disruptions limits the operational space of the tokamak. Under most conditions, the density [10] and current [11] limits are disruptive (although recent techniques such as boronization or the use of beryllium tend to make the density limit softer). Secondly, in particular at high current operation, the current quench following a disruption induces large currents in the vessel. The resulting electromagnetic forces can damage the mechanical structure, and only a limited number of hard disruptions can be tolerated during the life-time of a large tokamak. In addition, the intense heat flux during the disruption can damage limiters or divertor plates. It is therefore important to understand the mechanisms by which disruptions occur. Despite detailed experimental studies [1-9], the theoretical understanding has remained poor.

It is generally agreed that density limit disruptions are caused by radiative cooling of the outer regions of the plasma and the resulting contraction of the current channel. Once the current density at $q = 2$ is sufficiently low, the m=2/n=1 tearing mode becomes unstable [1-9]. Mode coupling [12,13] and quasi-linear [14] theories have been proposed in order to explain the subsequent evolution to major disruption in which almost all the thermal energy of the plasma is lost and the current profile broadens rapidly. In addition to the large m=2/n=1 mode, experimental observations also show an $m = 1$ deformation of the center just before the broadening of the current profile. This has been shown recently with high resolution measurements on JET [8] and T-10 [9], and similar observations have been made previously on T-4 [1], PLT [4], and JIPP T-II [6]. The role of the $m = 1$ relaxation is not explained by either the mode-coupling or quasi-linear theories. The accompanying MHD simulations also do not show a key signature of a major disruption, namely the pronounced and rapid broadening of the current profile.

The main result of the present simulation study is a model of the major disruption in which an internal instability with a predominantly $m = 1$ displacement occurs just before the final broadening of the current profile. The internal relaxation resembles a sawtooth crash, however, it is strongly modified by the presence of a large $q = 2$ helical perturbation which couples the m=1/n=1 mode to 3/2 and -1/0 components. The magnetic perturbation of the internal relaxation that initiates the major disruption is dominated by the m=3/n=2 component rather than m=1/n=1. At a late stage of the internal relaxation, the large amplitude 2/1, 3/2 and

1/1 perturbations stochasticize the magnetic field in the q = 1 island and at its end, the magnetic field is stochastic and the temperature profile flat in the region $q \leq 2$. Following the stochastisation, MHD turbulence develops with a filamentation and a broadening of the current profile in the $q \leq 2$ region. A broad spectrum of modes is excited and many intermediate- and high-m components are growing. However, the amplitude of the dominant m=2/n=1 mode remains almost constant during this phase. After a short delay, first the m=2/n=1 and later the m>2/n=1 modes start to grow very rapidly. In this final stage, the current profile broadens and the magnetic field becomes stochastic across the whole plasma cross section.

Our model combines the elements of interaction between the 2/1 and 1/1 modes of the quasi-linear model [14] with the mode coupling and turbulence of the mode coupling theory [12,13], although it differs from both in detail. It is also clearly different from a recent suggestion [15] that an internal disruption produces a hollow q-profile with central q-values of the order of 5 and that the subsequent development of an m=2/n=1 double tearing mode is the cause of major disruption.

The original aim of the present study was to see to what extent density limit disruptions in JET can be reproduced by a reduced MHD model [16] with simple assumptions about radiation and transport. To this end, we specify radiation losses according to measurements on JET [8] in an MHD-transport calculation and compute the resulting MHD activity. The model is briefly described in Sec. 2, and is discussed in detail in the Appendix. The following sections present simulation results. The time history of a density limit disruption is subdivided into radiative contraction (Sec. 3), minor disruptions (Sec. 4) and major disruption (Sec. 5). We give main emphasis to the major disruption. In Sec. 6, we compare the computational results for density limit disruptions to experimental data.

2. MODEL

The numerical model used here is the lowest order reduced MHD equations together with a simple transport model [16,17] and radiation losses. A detailed description is given in the Appendix, and here we only summarize the main features. The transport coefficients are chosen so as to be realistic for JET, however, the small dissipation terms resistivity, viscosity and perpendicular thermal conductivity are multiplied by a transport enhancement factor E in the range of 10^3. This serves the purpose of reducing the Lundquist number $S = \tau_r/\tau_A$ (where τ_r denotes the resistive diffusion time and τ_A the toroidal Alfvén time) to values that can be

simulated with an affordable resolution, while keeping the relation between various dissipative timescales the same as in JET. A loss term representing radiation is introduced in the energy equation and we have attempted to reproduce the measurements [8] of its temporal and spatial variation during shot 11051 in JET. The resistivity is computed from the neoclassical formula of Ref. [18] using the *local* electron temperature. In some cases, we have then discarded the $(m, n) \neq (0, 0)$ components of the resistivity. We refer to this as simulations *with* and *without* resistivity perturbations. The equilibrium ($m = n = 0$) components of the resistivity are always evolved in time.

The profile of perpendicular thermal conductivity was chosen so as to reproduce the temperature profile of shot 11051 before the radiative contraction. The plasma current is held constant in time corresponding to a q_{cyl} of 5. The accuracy of the reconstruction of the initial equilibrium is confirmed by good agreement of the internal inductance ($\ell_i^{sim} \approx 1.4$, compared with $\ell_i^{exp} \approx 1.35$) and the ohmic loop voltage (≈ 0.6 V in experiment and simulation).

In operating the code, we have studied the effect of turning certain 'knobs'. These knobs are

(i) peakedness of the radiation layer,

(ii) turning on/off the $(m, n) \neq (0, 0)$ perturbations of the resistivity, and

(iii) the transport enhancement factor E which has been varied from 500 to 5000.

The majority of the simulations have been made with 16 Fourier components in poloidal and toroidal angle. These are represented by filled circles in Fig. 1. In some cases, we have used 27 Fourier modes to improve on resolution. The extra modes are shown as open circles in Fig. 1.

3. RADIATIVE CONTRACTION

In the initial stage of a density limit disruption, the temperature profile contracts when the radiation losses approach 100 % of the input power. It is observed [8] that the radiation is peaked in a narrow layer at the edge of the plasma, and that the m=3/n=1 and m=5/n=2 modes become unstable when the radiation peak is close to the respective resonant surfaces. In the simulations, we find that certain conditions must be satisfied in order for these modes to reach the observed levels, or even to become unstable at all.

We compare here three different simulations of the radiative contraction phase, all made with an enhancement factor E = 2000. The first case has the resistivity perturbations turned

off, while the second and third cases include the perturbed resistivity. The second case has radiation losses prescribed according to the measurements reported in [8] with a half-width of about 20 cm. We shall refer to this as 'normal' radiation. In the third run, the radiation profile is 'enhanced', with twice the amplitude and half the width.

Without resistivity perturbations, the 3/1 mode remains stable during the profile contraction, even when the radiation is enhanced, and Δ'_{31} is negative (or at most close to zero). The stability of the 3/1 mode can be attributed to the peaking of the current profile by neoclassical resistivity. It is interesting to note that in simulations using Spitzer resistivity, the 3/1 mode is rather easily destabilized [14]. This appears to reflect experimental differences between JET and smaller tokamaks. It is well known that small tokamaks experience difficulties in crossing q = 3 because of instability of the m = 3 mode, and that the passage can be made safely only at low density [7, 19]. In JET, on the other hand, q = 3 can be crossed at higher density, provided only that the internal inductance is within a certain interval [8]. On the basis of our simulation results, the difference appears to be explained by the neoclassical peaking of the current profile in JET resulting from low collisionality and small aspect ratio.

With the resistivity perturbations included, the 3/1 mode does become unstable even though $\Delta'_{31} < 0$. With the normal radiation profile, the instability is weak and the radial magnetic field at the wall has a peak value of less than 2 G. Furthermore, the m=5/n=2 mode remains stable. On the other hand, with *enhanced radiation* and *perturbed resistivity*, the maximum in B_r is about 7 G which is close to the experimental observation ($\approx$ 9 G in shot 11051 [8]). In this case, the 5/2 mode also becomes unstable. Figure 2 shows the time evolution of the radial magnetic field for the 3/1, 5/2 and 2/1 modes for a run where the enhancement factor is E = 500, resistivity perturbations are included, and the radiation is twice as peaked as reported in Ref. [8]. The m = 3 signal reaches 9 G. Figure 3 shows the equilibrium (m = n = 0) profiles of the electron temperature T_e and current density j at the beginning of the simulation and at the time of maximum B_r for the 3/1 mode. Figure 4 shows contour plots of T_e and j at this time.

Comparison between the three simulations allows us to draw two conclusions. First, the resistivity perturbations are essential for reproducing the behavior of the resistive modes near the edge. In linear theory, these are destabilized by the 'rippling' mechanism [20]. It is generally agreed that rippling modes are stabilized at high temperature because of high thermal conductivity along the field lines. The simulation results are consistent with this, as the 3/1 and

5/2 modes are driven unstable when their respective resonant surfaces have already been cooled by the radiation front.

In nonlinear theory, resistivity perturbations contribute to growth of the magnetic islands by a thermal instability [21]. A decreased current density at the O-point of a magnetic island (assuming that the shear is positive) decreases the ohmic heating rate. Thus, for a large island, where the interior is thermally isolated from its surroundings, the O-point may become colder and the resistivity higher. The higher resistivity implies a lower current density at the O-point, and this contributes to make the island larger. Our simulations show that the thermal instability is of importance for modes with resonant surfaces in the cold edge region. (The dependence of the radiation losses on temperature, which is not correctly modeled by Eq. (A8), may enhance the thermal instability.)

Secondly, by comparing the saturated amplitudes of the 5/2 and 3/1 modes computed with different radiation profiles to the JET results, we are lead to the conclusion that the radiation peak is narrow, probably a factor of two narrower than reported [8]. This cannot be excluded experimentally, as the width of the radiation peak is comparable to the radial resolution of the bolometer [22].

Figure 4 shows that the q = 3 island leads to local flattenings of the temperature and current profiles and steepens the current gradient at the inner separatrix. Despite this, the 3/1 and 5/2 modes do not appreciably influence the temperature evolution in the bulk of the plasma at early times of the profile contraction. The decrease in plasma temperature at this time is mainly a direct consequence of the radiative cooling and the MHD activity does not play a major role until the m=2/n=1 mode becomes unstable.

4. MINOR DISRUPTIONS

When the radiation front approaches the q = 2 surface, the m=2/n=1 mode is strongly destabilized, and the q = 2 magnetic island grows quickly to between 10% and 20% of the minor radius. Linear calculations show values for $a\Delta'$ of the order of 10 or larger. Under these circumstances, the resistivity perturbations do not have a major effect on the evolution, as shown by Fig. 5. Figure 5 compares the 2/1 component of B_r at the wall for two cases which differ only in that the first includes the resistivity perturbations and the second does not. The case with perturbed resistivity shows a somewhat more rapid growth of the 2/1 mode, but in both cases B_r saturates at about 14 G. For numerical reasons, we are unable to compute with

parallel thermal conductivities for temperatures higher than 400 eV (see Appendix). Above this temperature, the thermal instability tends to be overestimated and, thus, is not correctly simulated in the hot central region. After the phase when the 2/1 mode gets excited, the most noticeable effect of the resistivity perturbations is destabilization of the m=1/n=1 mode, leading to more frequent internal disruptions than observed experimentally. However, the major disruption takes place by the same mechanism in the simulations, whether resistivity perturbations are included or not. The runs discussed in the following have the resistivity perturbations turned off.

Complete runs of density limit disruptions, including major disruption, have been made with transport enhancement factors of E = 1000, 2000, and 5000. The general behavior is similar for the three values of E. In all cases, a sequence of minor disruptions occurs before the final major disruption. The minor disruptions cause sharp drops of the plasma temperature mainly in the central region and lead to decreases of 0.1 to 0.2 in the internal inductance.

The simulated period τ_{md} of the minor disruptions, when measured in Alfvén times, increases almost linearly with the Lundquist number S, i.e., it scales with the resistive time. Consequently, the period measured on the transport time scale, $E \times \tau_{md}$, is almost independent of E. With this transport scaling, the simulations give the period of minor disruptions rather close to experimental observations. As an example, the run with E = 2000 gives a period of about 800 τ_A. Extrapolation to JET gives about 0.3 sec (800 × 0.2 μsec × 2000 = 0.3 sec) which is only a factor of 2 larger than the experimental value.

We now concentrate on the run with E = 5000, resistivity perturbations turned off and normal radiation profiles and discuss its time history in detail. This run includes all the 27 Fourier components shown in Fig. 1 and has the best resolved spectrum of all the simulations that we have made. The S-number is moderate, about 1.7×10^5 (computed from the initial central temperature). Figure 6 shows the time histories of the principal modes and other diagnostics. (a) shows the radial magnetic field B_r at the wall, (b) the square-root of the magnetic energy, W_M (indicating characteristic amplitudes of magnetic perturbations), (c) the logarithm of W_M and (d) the logarithm of the kinetic energy, W_K, of the principal modes. In addition, Fig. 6 shows the temporal evolution of (e) the electron temperature at three different radii, (f) the internal inductance ℓ_i and loop voltage V_ℓ and (g) the central safety factor q_0 (defined with respect to the current inside 16% of the minor radius).

A sequence of pronounced drops in the central temperature can be seen in Fig. 6 e. Two of these, occurring at $t/\tau_A \approx 2000$ and 2400, lead to decreases in the internal inductance of about 0.2. These characteristics are observed experimentally in minor disruptions.

4.1 Linear instability

The time history of the kinetic energies in Fig. 6 d shows that, during the minor disruptions at $t/\tau_A \approx 2000$ and 2400, the plasma displacement is predominantly m=1/n=1. In addition, the displacement is largest in the central region where $q \approx 1$, and we shall refer to these as $q = 1$ minor disruptions. Although the displacement is mainly m=1/n=1, the associated magnetic perturbation has an m=3/n=2 magnetic component that is at least as strong as the 1/1 component. The instability triggering the minor disruptions may be understood by considering the modification of the cylindrical eigenmodes in helical quasi-equilibria with large $q = 2$ islands. The eigenmodes on such equilibria involve all Fourier components with m - 2n = constant, and the mode of interest here has m = 2n - 1. We have carried out linear stability calculations for several $q = 2$ helical equilibria. These calculations show that the instability causing the $q = 1$ minor disruptions is driven by a combination of the normal driving force of the resistive internal kink mode (simply $q < 1$ at infinite aspect ratio) and that of the 3/2 tearing mode (current gradients inside the $q = 3/2$ surface). Unlike the resistive kink mode in a circular large aspect ratio equilibrium, the stability and mode structure depend continuously on q_0 around 1.

Figure 7 shows the location of the $q = 1$, 3/2, 5/2, and 3 resonant surfaces together with the $q = 2$ separatrix for the helical quasi-equilibrium at the start of a minor disruption, $t/\tau_A = 2383$. The perturbed stream and flux functions are shown in Fig. 8 in two opposite toroidal planes. The stream function resembles that of the m=1/n=1 internal kink, but it is modified by the elliptic deformation of the $q = 1$ surface caused by the $q = 2$ helical field. The distribution of magnetic and kinetic energies in the unstable eigenmode is shown in Fig. 9. It should be noted that the m=-1/n=0 component contributes a sizable fraction of the kinetic energy. In the magnetic energy, the m=3/n=2 component is dominant. In fact, the magnetic perturbation looks like the 3/2 tearing mode modified by the large $q = 2$ island. It has been shown previously [23] that a sufficiently large $q = 2$ island can even destabilize an *ideal* mode with 3/2 and 1/1 as its principal components.

4.2 Nonlinear development

Figure 10 shows the electron temperature and Fig. 11 the current density at four different times during a minor disruption. The peaks in magnetic and kinetic energies of the perturbations and the drop of central temperature and internal inductance are clearly seen in Fig. 6. Poincaré plots of the magnetic field lines at early times of the minor disruption ($t/\tau_A < 2410$) show flux surfaces in the central region with the same topology as that resulting from a normal internal kink mode. However, in the region around $q = 2$, the magnetic field lines are stochastic. Starting at $t/\tau_A \approx 2410$, the magnetic field lines inside the $q = 1$ island become stochastic very rapidly. (This is shown in detail in Sec. 5.1.) The stochastisation is different from the normal behavior of a sawtooth crash (as found in MHD simulations [17, 24]). It is caused by the excitation of a strong 3/2 component by the nonlinear coupling of 1/1 and 2/1. After breakup of the magnetic surfaces in the $q \approx 1$ region (Fig. 10 c), the magnetic field is stochastic in the entire region $q \leq 2$ and the temperature flattens over this region, see Fig. 10 d. (The temperature flattening ends when the magnetic surfaces heal again, which happens quite rapidly for this large resistivity enhancement factor. With a smaller enhancement factor, the temperature flattening has time to become more complete than in Fig. 10 d.)

A consistent feature of the minor disruptions is that there is always one toroidal plane in which the O-points of the $m/n = 1$, 3/2 and 2 magnetic islands align. In our cylindrically symmetric configuration, the angle of alignment is arbitrary. However, at finite aspect ratio, we expect toroidal coupling to determine the poloidal angle at which the modes align [3].

The plot of the current density in Fig. 11 c shows that following the stochastisation, turbulent fluctuations of the current density occur in the region of steep current gradients just outside the $q \approx 1$ region. This MHD turbulence develops because the stochastic magnetic fields lead to violation of the equilibrium condition that the current density be constant on a field line. When there are no intact flux surfaces left that isolate the $q \approx 1$ region of high current density from the region outside with a small current density, the plasma can no longer remain in equilibrium. It may be seen from Fig. 6 c, d that there is a slight secondary peak in the energies of several Fourier components at $t/\tau_A \approx 2500$. In a major disruption, such induced instabilities reach a much higher amplitude and completely rearrange the current profile.

It is clear from Fig. 6 g that one nonlinear consequence of the minor disruptions is to raise the central q-value. This is similar to the result of a normal sawtooth crash. The period of the minor disruptions in the simulations is about twice the sawtooth period before the profile

contraction. Therefore, the minor disruptions reconnect a larger magnetic flux and give rise to larger changes in q_0. The ratio of periods between minor disruptions and sawteeth in JET shot 11051 is about 3. The increase in period may be explained by the larger inversion radius for the minor disruptions. This is due to the contracted current profile for which more current flows in the central region. Figure 6 b shows that the amplitude of the 2/1 mode increases after each minor disruption, evidently as a consequence of changes in current distribution induced by the minor disruptions. It is well known that the m=2/n=1 mode is destabilized by increases in q_0.

4.3 Role of mode coupling

In discussing the q = 1 minor disruptions, we have emphasized the importance of mode coupling resulting from the large amplitude m=2/n=1 mode. This point can be demonstrated very clearly by excluding the m=1/n=0 Fourier component from the simulation. Figure 12 shows the time history of central temperature and internal inductance for two runs with an enhancement factor of 2000. The two runs are identical except that in Fig. 12 b the m=1/n=0 Fourier component was removed at $t/\tau_A = 5847$. The minor disruptions with marked drops in T_0 and ℓ_i are then replaced by m=1/n=1 activity with a shorter period, and each relaxation gives much smaller drops in T_0 and particularly in ℓ_i. This very special truncation of the spectrum proves that the m=1/n=0 mode is important. Since this mode does not have a resonant surface in the plasma, we conclude that mode coupling plays a significant role. This conclusion is also supported by the strong modification of the internal kink mode due to the q = 2 fields, as shown in Figs. 8 and 9. Consequently, the minor disruptions cannot be accurately described by quasi-linear theory. We note that the 1/0 mode was not included in a previous (and unsuccessful) attempt to simulate major disruptions [16].

5. MAJOR DISRUPTION

Experimentally, a major disruption leads to an almost complete loss of the thermal energy and flattens the current distribution. In the simulation, the internal inductance falls from about 2 to 1.1 between 2800 and 2950 τ_A (see Fig. 6 f), and we identify this as a major disruption. This phase shows a complex sequence of events. In an attempt to describe the evolution (perhaps in a somewhat oversimplified way) we can identify two main phases of the

major disruption: an internal relaxation similar to the q = 1 minor disruptions followed by filamentation and broadening of the current profile.

The time histories of the magnetic and kinetic perturbation amplitudes are shown in Fig. 13 on a linear scale. The electron temperature, current density and stream function at several times during the major disruption are shown in Figs. 14 - 18 and Fig. 19 shows Poincaré plots of the magnetic field.

5.1 Internal relaxation

The first event taking place from about 2710 τ_A to 2810 τ_A is an internal relaxation of the same nature as the minor disruptions, although more violent. The Poincaré plots 19 a, b at 2714 τ_A and 2764 τ_A show that during the first part of the internal relaxation, well-defined flux surfaces exist and have the standard island structure of a q = 1 reconnecting internal kink mode. However, the field line structure gets significantly distorted by the coupling to the 2/1 and 3/2 modes. This is shown by the Poincaré plot in Fig. 19 b, soon before the q ≈ 1 region is stochasticized. The similarity to a sawtooth can also be seen from the predominantly m=1/n=1 convection pattern in Fig. 14 c. At a later stage of the internal relaxation, at about 2790 τ_A, the evolution is clearly different from that taking place during a normal sawtooth crash. The isolating magnetic surfaces between the cold q = 1 island and the stochastic region around q = 2 are broken up and the q = 1 island is rapidly stochasticized, see Fig. 19 c. The temperature plot 15 a shows a cold spot in the q ≈ 1 region, opposite to the hot core, and the 1/1 and 2/1 vortices in the convection pattern (Fig. 15 c) appear to mix near this cold spot. As in the minor disruptions, the O-points of the 1/1, 3/2 and 2/1 islands line up in a certain toroidal plane. Figures 14 - 19 show the plane 90 degrees away toroidally from this symmetry plane.

After stochastisation of the q = 1 island, MHD turbulence starts to develop. This is most clearly visible in the current density, Figs. 15 b and 16 b. The hot core around the old magnetic axis continues to be annihilated by a combination of reconnection driven by the m = 1 flow and stochastisation due to the turbulence, cf Figs. 15 a and 16 a.

In [8], the internal relaxation was described as a 'profile erosion', interpreted as being due to stochastisation of the magnetic field rather than to a fluid displacement. This conclusion was supported by line averaged X-ray emissivities. The internal relaxation in the present simulation shows a somewhat different nature, and at least during its first part (Figs. 14 and 19 a, b), it is connected with a fluid displacement, stochasticity occurring mainly toward the end

(Figs. 15 and 19 c). Recently performed two-dimensional tomographic reconstructions of the JET data [25] show X-ray emission profiles during the final internal relaxation that are initially flat in the center (similar to the temperature profile in the simulation around 2700 τ_A) and later take the form of a double step. These profiles are consistent with the interpretation of erosion [8]. However, they are also reproduced by the present simulations, where the temperature profile in the central region first evolves by fluid motion starting from a centrally flat initial condition.

5.2 Current broadening

5.2.1 Filamentation in the central region

The simulations show only quantitative differences between the final internal relaxation and the minor disruptions. Comparison between the mode amplitudes during the major disruption and those during the minor disruption that precedes it (see Fig. 6 b) shows that the m=1/n=1 mode reaches a slightly higher amplitude in the final internal relaxation, and a more significant difference occurs in the 3/2 magnetic energy. The q = 1 island gets stochasticized around 2790 τ_A, see Fig. 19 c. After this, the current density develops filaments in the region of strong current gradients. In contrast with the minor disruptions, the current filamentation continues to grow and persists until the end of the major disruption, as shown by Figs. 16 b - 18 b.

Following the internal relaxation (soon after Fig. 15 at $t/\tau_A = 2795$), the temperature profile is almost stationary until $t/\tau_A \approx 2870$ (see Fig. 16 a), and the most clearly visible sign of MHD activity is filamentation of the current. Although a broad spectrum of Fourier components is excited and growing in time, the dominant m=2/n=1 mode remains approximately stationary during this period. The current filamentation is restricted to the central region $q \leq 2$, where the magnetic field is completely stochastic. The stream function in Fig. 16c shows a rather localized vortex which mainly involves Fourier components 1/1, 2/1 and 3/2. The loop voltage is small and negative, as in the minor disruptions.

5.2.2 Rapid growth of m≥2 / n=1 modes

The turbulent current fluctuations in the central region grow steadily after the internal relaxation. At a certain point, when the central region has become thoroughly turbulent and the current profile sufficiently rearranged, the m=2/n=1 mode starts to grow rapidly. In a single helicity projection, the q = 2 island grows to encompass the whole central region between $2870\tau_A$ and $2910\ \tau_A$ (cf. Figs. 16 and 17). Soon thereafter, the m=3/n=1 and the m=4/n=1 modes grow even more rapidly, almost on an Alfvénic timescale. The excitation of these modes can be understood as a quasilinear effect of the broadened current profile with central q above 2. The high growth-rates are possible because the respective resonant surfaces are cold. The stream function is now turbulent, and at least the m = 1, 2 and 3 components can be distinguished in Figs. 17 c and 18 c. (In simulations at higher S-number, the flow pattern shows eddies over a wider range of spatial scales.) After the m=3/n=1 and m=4/n=1 modes have reached high amplitude, the magnetic field is stochastic across the entire cross-section, as shown by Fig. 19 d.

Similar to the minor disruptions, the different modes phase lock during the final phase. Here, the locking consistently leads to alignment of the O-points of the 2/1, 3/1 and 4/1 modes in one toroidal plane (and of the X-points in the opposite toroidal plane).

The gross shape of the current profile is quantified by the internal inductance. Figure 6f shows that the broadening of the current profile takes place mainly during the final phase, when the 2/1, 3/1 and 4/1 modes are rapidly growing. During this phase, the loop voltage becomes strongly negative (see Fig. 6 f). As noted previously [26], the negative spike in the loop voltage occurs late in the disruption sequence. In the simulation, the maximum negative loop voltage occurs at the time when the m=4/n=1 mode reaches high amplitude. Our simulations support the interpretation in [26] that the rearrangement of the current profile starts in the center and reaches the edge only at a late stage. Figures 15 b - 18 b show that regions of negative current density form at increasing distance from the center during the second phase of the major disruption.

5.2.3 What makes a disruption major ?

In comparing the minor disruption at about $2400\ \tau_A$ depicted in Figs. 10 and 11 with the similar internal relaxation at $2750\ \tau_A$ (Figs. 14 - 18), it is natural to ask why the latter leads to

major disruption and the former does not. From an analysis of several simulations at different S-values, there appears to be a sharp threshold that determines whether a minor disruption will continue into a major disruption or not. When the isolating good flux surfaces between the regions of high and low current density are destroyed, the equilibrium condition that the current be constant on a field line is violated. Therefore, either the stochastic fields must be eliminated, or violent MHD activity must follow. The former case means that the discharge recovers, in other words, the disruption is minor, and the latter case leads to elimination of the current gradients, i.e., to major disruption.

As far as we have been able to determine, the first clear sign that a major disruption will occur is strong excitation of the 3/2 mode. This criterion is clearly illustrated by comparison of the last minor disruption and the major disruption in Fig. 6 b. The continued evolution is much influenced by the 3/2 mode, and it appears that the sharp threshold can be explained by the highly nonlinear character of the major disruption. According to the previous discussion, the major disruption takes place through a sequence of several nonlinear events: (a) 1/1 + 2/1 $\rightarrow$ 3/2, (b) 1/1 + 3/2 + 2/1 $\rightarrow$ stochasticity, turbulence and profile modification and, finally, (c) the $m \geq 2/n=1$ modes grow explosively resulting in complete stochastisation and current profile broadening. In a minor disruption, the m=3/n=2 perturbation generated in the first step is weaker than in a major disruption, either because the 2/1 mode is smaller or the 1/1 instability is weaker. This leads to less turbulence in phase (b) and the ensuing growth of the 2/1 mode in phase (c) is slow and weak. The long sequence of events, each a nonlinear consequence of its predecessor and involving the 2/1 mode, is consistent with a very sharp threshold in the 2/1 amplitude for major disruption to occur. This threshold character seems to be corroborated by experimental observations of density limit disruptions in JET.

6. COMPARISON WITH EXPERIMENT

The simulation presented in Secs. 3 - 5 shows many of the characteristics found experimentally in density limit disruptions on JET and other tokamaks. Simulations performed at 2.5 and 5 times higher S-number show the same qualitative behavior, although the numerical resolution during the major disruption is less convincing. Among the experimental phenomena reproduced successfully by the simulations we note:

(a) instability of the 3/1 and 5/2 modes during the profile contraction phase

(b) saturation of the n = 1 component of B_r at the wall at 14 - 15 G, close to the 16 - 18 G [8] observed in JET shot 11051

(c) a sequence of minor disruptions

(d) major disruption taking place in two steps

(e) a first phase of the major disruption where an internal relaxation of predominantly m = 1 character flattens the central temperature

(f) a second phase of the major disruption in which the current profile broadens. After a short delay from the internal relaxation, the m = 2, 3, 4 / n = 1 modes grow rapidly.

The reproduction of these features in the simulation is surprisingly detailed, given the simplicity of the reduced MHD model and the reduction of the S-number by a factor ranging from 1000 to 5000. However, there are clear uncertainties concerning the accuracy of the model equations, and the theoretical model can only be justified after careful comparison with experiment. Of course, the most challenging comparison concerns the major disruption itself.

The internal relaxation that starts the major disruption was interpreted in Ref. [8] as the result of magnetic field stochastisation only. Our simulation model shows an m = 1 convection pattern with stochasticity playing an important role only toward the end of the internal relaxation. The interpretation of Ref. [8] was supported by *line averaged* X-ray emissivities. However, our convection model is consistent with recent *tomographic reconstructions* [25] fully explaining the erosion-like behavior. Both our simulation results and the tomographic reconstruction show a temperature profile that is initially *flat* in the center, close to a step-function, and the continued evolution gives rise to a profile in the form of a double step, see Fig. 15 a.

Another comparison can be made between the experimental measurement of the n = 1 radial magnetic field at the wall, shown in Fig. 20, and simulation results for the magnetic perturbation amplitude during the disruption, see Fig. 13. The separation into two distinct growth phases, one during the internal relaxation and one during the final current broadening and negative voltage spike, is evident in both cases. (The magnetic field at the wall does not vary much during this time in the simulation because the time constant of the wall is too long, $\tau_w = 1000\ \tau_A$.)

Despite the successful reproduction of many experimental events, certain other features are missing in the simulations. One missing feature is the so called energy quench that occurs

during the final increase in the radial magnetic field and brings the electron temperature to very low values. At the end of the major disruption, the computed current profile is flattened and the magnetic field becomes stochastic across the entire plasma. By tracing field lines, we find that it takes on the order of fifty toroidal turns for a typical field line to make a radial excursion comparable to the minor radius. An electron with 300 eV energy in the parallel direction traverses this distance in about 100 μs (i.e., 500 Alfvén times) in JET. When the effects of collisions are taken into account, the timescale for conduction along the field lines is increased. Because of the large resistivity enhancement factor in the simulations, the resistive MHD activity is sped up so that the flux surfaces have time to heal again during the time required for the electrons to leave the plasma along the ergodic field lines. Consequently, the simulations fail to produce a final drop of the temperature to very low values.

It should be noted that somewhat different data concerning energy quench have been reported from different experiments. JET discharges with carbon limiters show drops of the electron temperature to about 10 eV in a time of the order of 250 μs [8]. On the other hand, in TFR with metal limiters [5], the electron temperature falls to about 200 eV in less than 1 ms and then evolves slowly. While the TFR result can be explained by conduction along stochastic field lines, it appears that atomic physics effects play an important additional role for the temperature evolution during the thermal energy quench in JET. This is not modeled in our MHD simulations.

Careful examination of the X-ray and ECE data from JET reveals that there are at least two types of minor disruptions, connected mainly with the $q = 1$ and $q = 2$ surfaces, respectively. These different types of minor disruptions were noted already in early measurements on PLT [4]. Our simulations show minor disruptions only of the $q = 1$ type, with the single exception of that caused by the initial growth of the m=2/n=1 mode (at $t/\tau_A \approx$ 1400 in Fig. 6).

Probably, a more significant difficulty is the extrapolation to S-values characteristic of JET. One obvious problem stems from the fact that the $q = 1$ minor disruptions show some similarity to the sawtooth crashes. Thus, it may be argued that the simulation model must be able to reproduce sawteeth in JET. It has been shown [17] that the resistive reduced MHD model successfully reproduces sawteeth in small tokamaks (say $S < 10^7$) but not at S-values relevant for JET, where toroidal effects significantly modify the sawtoothing [24]. However, in the present simulations, the effects of the $q = 2$ helical deformation on the internal disruptions are more important than toroidicity, and these effects are retained in the reduced MHD model.

With regard to the timescales for reconnection to occur at high S-numbers, it has been pointed out that the fast sawtooth crashes observed in JET and TFTR are inconsistent with *resistive* reconnection, unless a strongly anomalous resistivity is invoked [24, 27]. In addition, it has been shown recently that a significant increase over resistive reconnection rates at high values of S results from *collisionless* reconnection, by electron inertia [28]. As an example of the difficulties in extrapolating the time-scales of our simulations to JET, we consider the time interval between the peak of the 1/1 mode during the internal relaxation and that of the 2/1 mode during the current flattening (see Fig. 13). For the simulations with resistivity enhancement factors of E = 5000, 2000, 1000 these times are about 140, 230, and 390 Alfvén times, respectively. If we try to fit a power law, the result is $\Delta t / \tau_A \approx 3 \times 10^4 \, (S/S_{JET})^{0.63}$. This expression gives a time delay between the end of the internal relaxation and the final increase in B_r of about 6 ms for JET. Although time delays of this length are sometimes observed, a more typical value is 2 ms (as in Fig. 20). Thus, it appears that the activity during the major disruption is faster than the resistive MHD prediction. This could be due to electron inertial effects and/or to anomalous resistivity. It does not imply that there is a fundamental ('topological') change in the nature of the instability mechanism, cf. the discussion of sawtooth oscillations [17, 24, 27-29]. Work including electron inertial effects in the present simulation code is underway.

7. CONCLUSION

To conclude, we summarize the simulation results concerning the mechanism of density limit disruption. The disruption follows a radiative contraction of the current profile. Early during the profile contraction, MHD modes with resonant surfaces near the plasma edge are destabilized, and later the m=2/n=1 mode grows to a large amplitude. After the initial growth of the m=2 mode, a sequence of minor disruptions follows. The q = 1 minor disruptions are triggered by an instability of the helical q = 2 quasi-equilibrium in which the 1/1 mode gets strongly coupled to its 3/2 and -1/0 side-bands.

The major disruption takes place in two phases. The first phase is an internal relaxation, similar to a q = 1 minor disruption, that flattens the temperature over a large part of the plasma. The final internal relaxation differs from the preceding minor disruptions only in magnitude, most notably in the 3/2 magnetic perturbation. At the end of the internal relaxation, the magnetic field is stochastic across the entire region $q \leq 2$. In the second phase, MHD

turbulence develops, initially on the sharp current gradient between the $q \approx 1$ region and the q=2 magnetic island. This MHD turbulence involving intermediate- to high-m modes leads to a filamentation and broadening of the current profile in the $q \leq 2$ region. During this internal current redistribution, the m=2/n=1 mode amplitude stays essentially constant. After the central current profile has broadened sufficiently, the m=2/n=1 amplitude increases sharply. The current profile now broadens over a larger region. The disruption is completed by a rapid instability of the m=3, 4/n=1 modes and the magnetic field becomes stochastic across the whole plasma. During this last phase, a negative pulse appears in the loop voltage. The sequence of events described here is in accord with experimental results for major disruption in JET and is also close to the description given early by Mirnov and Semenov [1].

As a final comment, we note a close connection between our model of density limit disruption and a recent model suggested for high-beta disruption [29]. In both cases, the major disruption is triggered by an internal kink mode (predominantly m=1/n=1) becoming unstable. The nonlinear evolution of the instability leads to stochastic magnetic fields via mode coupling. In the case of high-beta disruption, the mode coupling is provided by toroidal high-beta effects on the equilibrium, whereas in our model of density limit disruption, the mode coupling is due to the helical deformation by a large amplitude m=2/n=1 mode. We expect that the mechanism for major disruption described here also applies to current limit disruptions, although the triggering of the m=2/n=1 mode is different in this case [11].

ACKNOWLEDGEMENT

This research was supported in part by JET contract JW8 / 9007 and by the Fonds National Suisse pour la Recherche Scientifique. The computations have been carried out on the CRAY-2 computer at EPFL, and we are grateful for the excellent service provided by the Service Informatique Central . We are pleased to acknowledge helpful discussions with Drs. D. Bartlett, D. Campbell, A. Edwards, R. Gill, N. Gottardi, P. Morgan, A. Pochelon, P. Smeulders and F. Tibone.

Appendix. Detailed description of simulation model

The numerical simulations presented in this paper have been made using a development of the code used in [16] and [17]. The following set of equations is evolved in time: the lowest order reduced MHD equations [30] (in normalized units),

$$\frac{\partial \psi}{\partial t} = \mathbf{B} \cdot \nabla \phi - \eta j + E_z(t) \quad , \tag{A1}$$

$$\left(\frac{\partial}{\partial t} + v_\perp \cdot \nabla\right) \omega = \mathbf{B} \cdot \nabla j + \nu \nabla^2 \omega, \tag{A2}$$

together with an equation for the electron temperature

$$(3\alpha/2)\left(\frac{\partial}{\partial t} + v_\perp \cdot \nabla\right) nT = \eta j^2 - P_{rad} + \nabla_\perp \cdot n\chi_\perp \nabla_\perp T + \mathbf{b} \cdot \nabla\, n\chi_{||}\, \mathbf{b} \cdot \nabla T \ . \tag{A3}$$

In (A1) and (A2), ϕ is the stream function, $v_\perp = \nabla\phi \times \nabla z$ is the fluid velocity, $\omega = -\nabla^2\phi$ is the vorticity, ψ is the magnetic flux function, $\mathbf{B} = B_T \nabla z + \nabla\psi \times \nabla z$ is the magnetic field, $\mathbf{b} = \mathbf{B}/B_T$, and $j = -\nabla^2\psi$ is the toroidal current density. The resistivity η is computed from the neoclassical formula of Hirshman et al [18]. At the vacuum-plasma interface, $r = a$, ψ is matched to a vacuum solution, with a resistive wall placed at $r = b = 1.15a$. In the simulations presented here, the time is given in units of the toroidal Alfvén time τ_A and the wall time for a mode with poloidal mode number m is $(1000/|m|)\ \tau_A$. The limiter at $r = a$ is modeled by a free-slip rigid wall boundary condition.

In the energy equation (A3), the coefficient $\alpha = 1 + 1/Z_{eff}$ represents thermal equilibration between electrons and ions. To model shot 11051 in JET, we choose $Z_{eff} = 1.8$. The particle density is held fixed in time

$$n(r) = n_0 \left(1 - r^2/r_0^2\right) \ , \qquad r_0 = 1.10\ a \tag{A4}$$

The perpendicular thermal conductivity is chosen so that the temperature profile at steady state and in the absence of radiation matches the corresponding profile on shot 11051. A good approximation is obtained with (in MKS units)

$$\chi_\perp = \begin{cases} 0.17\ m^2/s & r < 0.30a \\ 0.17 + 1.17\ (r/a - 0.30)\ \ m^2/s & r > 0.30a \end{cases} \qquad (A5)$$

The viscosity ν in Eq. (A2) is set equal to $\chi_\perp$ at half-radius r = 0.5a. The parallel thermal conductivity $\chi_{//}$ is taken according to classical collisional theory

$$\chi_{//}\ [m^2/s] = 1.91 \times 10^{23}\ T_e^{5/2}\ [eV] / n[m^{-3}] \qquad (A6)$$

However, as the parallel thermal conductivity becomes very large at high temperature, it has been necessary to introduce a cut-off so that $\chi_{//}^{sim} = \chi_{//}^{phys}(\min(T,T_0))$ with $T_0 = 400$ eV.

In practice, simulation using realistic values of the transport coefficients for a large tokamak such as JET is far too demanding, and the ratio S (Lundquist number) between the resistive and Alfvén time-scales has to be reduced. As a practical recipe [17], we multiply all the small dissipation coefficients by a transport enhancement factor E,

$$(\eta,\ \nu,\ \chi_\perp)^{sim} = E \times (\eta,\ \nu,\ \chi_\perp)^{phys}. \qquad (A7a)$$

This factor then gives the reduction of the ratio between transport and ideal-MHD timescales,

$$t^{phys}_{transport} = E \times t^{sim}_{transport}. \qquad (A7b)$$

It may be useful to give one example. The Alfvén time in JET (for shot 11051) is about 0.2 μsec. Thus, with an enhancement factor of 2000, 1000 Alfvén times in the simulation correspond to 0.2 μsec × 1000 × 2000 = 0.4 sec on the transport time-scale.

The radiation losses P_{rad} are prescribed so as to model the observed time-evolution during shot 11051. We write P_{rad} as the product of a prescribed function and a function of the plasma temperature that vanishes for T = 0, to ensure that the temperature stays positive,

$$P_{rad}\ (r, t, T) = P_{max}(t)\ \frac{1}{2}\ (1 + \tanh\ \frac{r - r_c(t)}{w(t)}\ )\ F(T)\ , \qquad (A8a)$$

$$F(T) = \begin{cases} 1 \quad , & T > T_c \ , \\ 2\,(T/T_c) - (T/T_c)^2 \ , & T < T_c \ , \end{cases} \tag{A8b}$$

with T_c = 200 eV. The width, w, is held fixed at 8 cm. The other parameters: amplitude, P_{max}, and radial position of the front, r_c, are prescribed so that (A8) matches measurements from shot 11051 at certain times. Between these times, the parameters are interpolated linearly. The times and the corresponding values of P_{max} and r_c are shown in Table I. [Note that the shortening of the transport time-scale in the simulations implies that the radiated power must be multiplied by the enhancement factor, thus $P_{rad}^{sim}(r,t^{sim}) = E \times P_{rad}^{phys}(r, Et^{sim})$.]

Normally, the code is run in such a way that the plasma current is held fixed in time by adjusting the toroidal electric field $E_z(t)$. This is appropriate in the case of slow evolution, where the plasma current is maintained at a preprogrammed value by a feedback system. However, during the rapid broadening of the current distribution and decreasing internal inductance in a major disruption, the control system is too slow to respond, and the plasma current increases at the moment of major disruption.

The interpretation of most code diagnostics is immediately clear, except, perhaps, for the loop voltage, V_ℓ. In Eq. (A1) the m=0/n=0 component of ψ is made to satisfy the boundary condition $\psi = 0$ at r=a. As a consequence, E_z multiplied by $2\pi R$ is the voltage in a set of toroidal loops, *on the plasma surface,* averaged over poloidal location. This is a good approximation for the corresponding experimental signal as long as the flux loops are close to the plasma surface and are not strongly affected by axisymmetric displacements. As the plasma current is held constant in the simulations, the spike in the loop voltage during major disruption is a consequence of rapid changes in the transformer flux only, and not of changes in plasma current, as in the experiment. However, it can be shown that the difference in V_ℓ is small if the magnetic coupling factor between the plasma and the flux loops is close to unity.

A finite difference scheme is used in the radial direction and Fourier decomposition in the angular directions. In all cases shown here, we have used 150 equidistant radial points and 16 to 27 Fourier components, see Fig. 1. No symmetry of the solution is assumed, i.e., each Fourier mode for ϕ and ψ has both the cosine and sine component. Furthermore, because the configuration space variables are real, there is symmetry about the origin in Fourier space, and it is sufficient to represent the modes with $n > 0$, m arbitrary and $n = 0$, $m \geq 0$.

REFERENCES

[1] MIRNOV, S.V., SEMENOV, I.B., in Plasma Physics and Controlled Nuclear Fusion Research 1976 (Proc. 6th Int. Conf. Berchtesgaden, 1976), Vol 1, IAEA Vienna (1977), 291.

[2] KARGER, F., LACKNER, K., FUSSMAN, G., et al, ibid, Vol 1, 267.

[3] EQUIPE TFR, Nucl. Fusion **17** (1977) 1283.

[4] SAUTHOFF, N.R., von GOELER, S., STODIEK,W., Nucl. Fusion, **18** (1978) 1445.

[5] TFR GROUP, "Major and Minor Disruptions in the TFR Tokamak", EUR-CEA-FC-1151, Nov. 1982.

[6] TSUJI, S., NAGAYAMA, Y., MIYAMOTO, K., KAWAHATA, K., NODA, N., TANAHASHI, S., Nucl. Fusion **25** (1985) 305.

[7] ALLADIO, F., BARDOTTI, G., BARTIROMO, R., et al, Nucl. Fusion **26** (1986) 11.

[8] WESSON, J.A., GILL, R.D., HUGON, M., et al, Nucl. Fusion **29** (1989) 641.

[9] KISLOV, D.A., LYADINA, E.S., RAZUMOVA, K.A., SAVRUKHIN, P.V., in Controlled Fusion and Plasma Physics (Proc. 17th Eur. Conf. Amsterdam, 1990), Vol 14B, Part I, European Physical Society (1990) 315.

[10] REBUT, P.H., GREEN, B.J., in Plasma Physics and Controlled Nuclear Fusion Research 1976 (Proc. 6th Int. Conf. Berchtesgaden, 1976), Vol 2, IAEA Vienna (1977) 3.

[11] BONDESON, A., PERSSON, M., Nucl. Fusion **28** (1988) 1887.

[12] WADDELL, B.V., CARRERAS, B., HICKS, H.R., HOLMES, J.A., Phys. Fluids **22** (1979) 896.

[13] DIAMOND, P.H., HAZELTINE, R.D., AN, Z.G., CARRERAS, B.A., HICKS, H.R., Phys. Fluids **27** (1984) 1449.

[14] TURNER, M.F., WESSON, J.A., Nucl. Fusion **22** (1982) 1069.

[15] KLEVA, R.G., DRAKE, J.F., DENTON, R.E., Comments on Plasma Phys. and Contr. Fusion **XIII** (1989) 63.

[16] BONDESON, A., Nucl. Fusion **26** (1986) 929.

[17] VLAD, G., BONDESON, A., Nucl. Fusion **29** (1989) 1139.

[18] HIRSHMAN, S.P., HAWRYLUK, R.J., BIRGE, B., Nucl. Fusion **17** (1977) 611.

[19] POCHELON, A., private communication (1989).

[20] FURTH, H.P., KILLEEN, J., ROSENBLUTH, M.N., Phys. Fluids **6** (1963) 459.

[21] REBUT, P.H., HUGON, M., in Plasma Physics and Controlled Nuclear Fusion Research 1984 (Proc. 10th Int. Conf. London 1984) Vol.2, IAEA, Vienna (1985) 197.

[22] GOTTARDI, N.A.O., private communication (1989).

[23] BONDESON, A., Phys. Rev. Lett. **51** (1983) 1668.

[24] PARK, W., MONTICELLO, D.A., Nucl. Fusion **30**, 2413 (1990).

[25] SMEULDERS, P., private communication (1990).

[26] WESSON, J.A., WARD, D.J., ROSENBLUTH, M.N., Nucl. Fusion **30** (1990), 1011.

[27] AYDEMIR, A.Y., Phys. Fluids **2B** (1990) 2135.

[28] WESSON, J.A., "On Sawtooth Reconnection", Post deadline paper presented at 13th IAEA Conf. Washington D.C., 1990.

[29] PARK, W., et al, "3D-MHD Studies of Sawtooth Oscillations and Pressure Driven Resistive Modes in Tokamaks", Paper D-2-5, 13th IAEA Conf., Washington D.C., 1990.

[30] STRAUSS, H.R., Phys. Fluids **19** (1976) 134.

TABLE I Values of P_{max} and r_c characterizing the radiation profile (see Eq. (A8)) at different times.

t (s)	P_{max} ($\times 10^4$ W.m^{-3})	r_c (m)
0.0	0.0	1.036
0.717	5.89	0.862
0.997	8.19	0.794
1.177	9.44	0.665
1.417	15.24	0.620
1.477	11.35	0.693
1.677	12.16	0.746
1.777	17.31	0.616
> 1.777	17.31	0.616

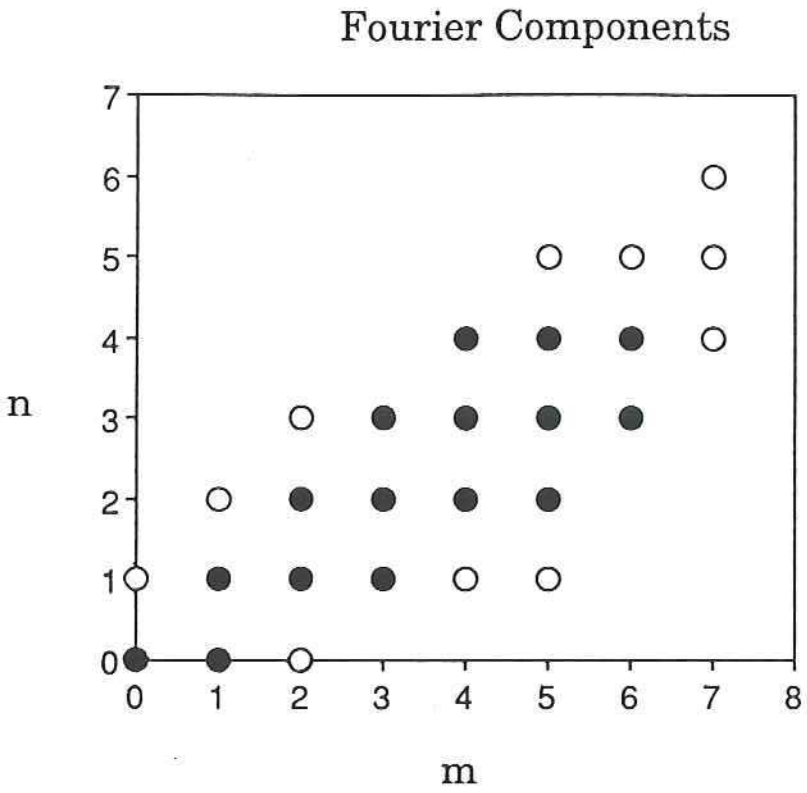

FIGURE 1 Fourier components included in the simulation. The 16 modes shown as filled circles are used in all cases. The 11 open circles show additional modes included in the simulation discussed in Secs.4 and 5.

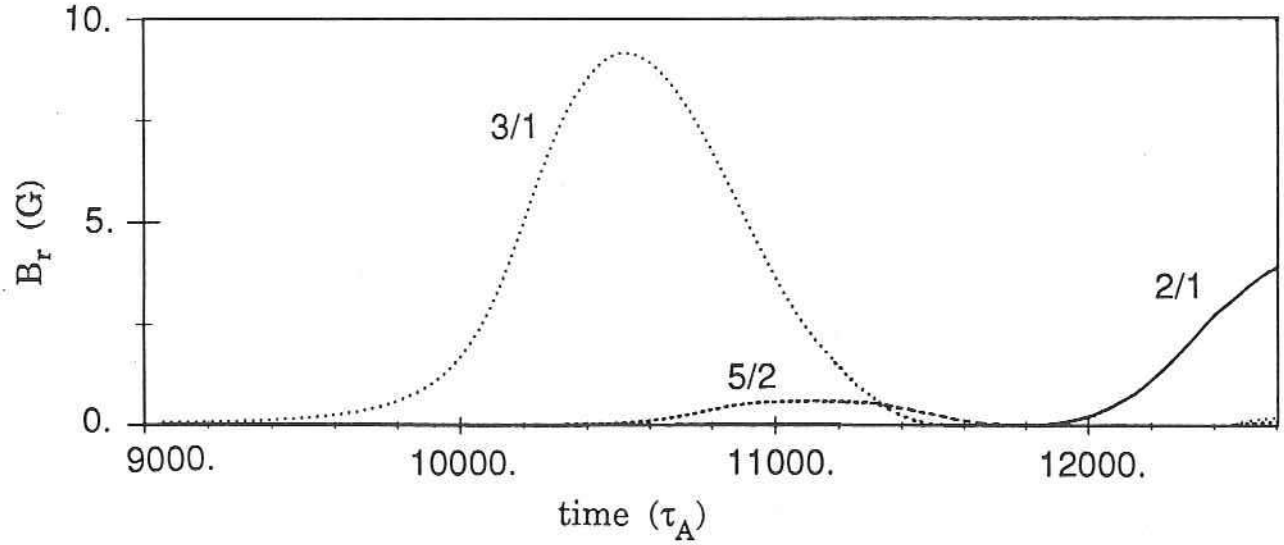

FIGURE 2 Time evolution of radial magnetic field at the wall for the 3/1, 5/2, and 2/1 modes during the profile contraction phase. This run was made with resistivity perturbations, enhanced radiation and E = 500.

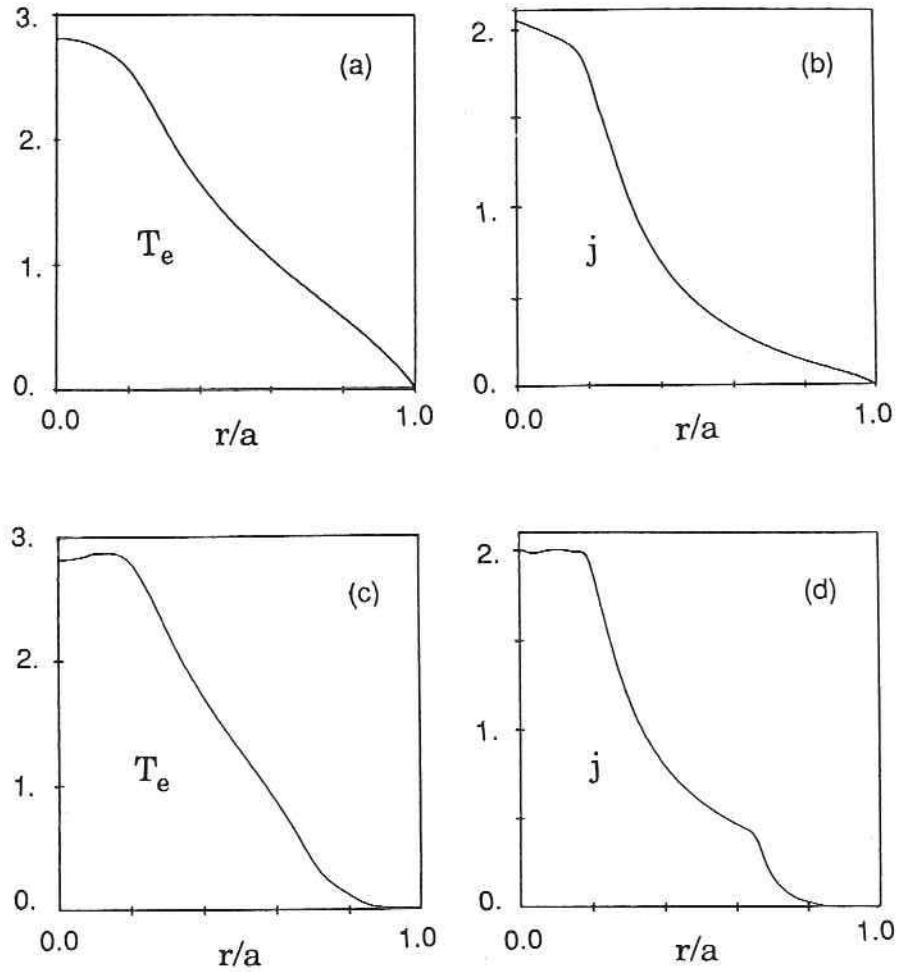

FIGURE 3 Radial profile of equilibrium (m = n = 0) electron temperature T_e and current density j; (a) and (b) before profile contraction and (c) and (d) at the time of maximal 3/1 amplitude during the initial profile contraction.

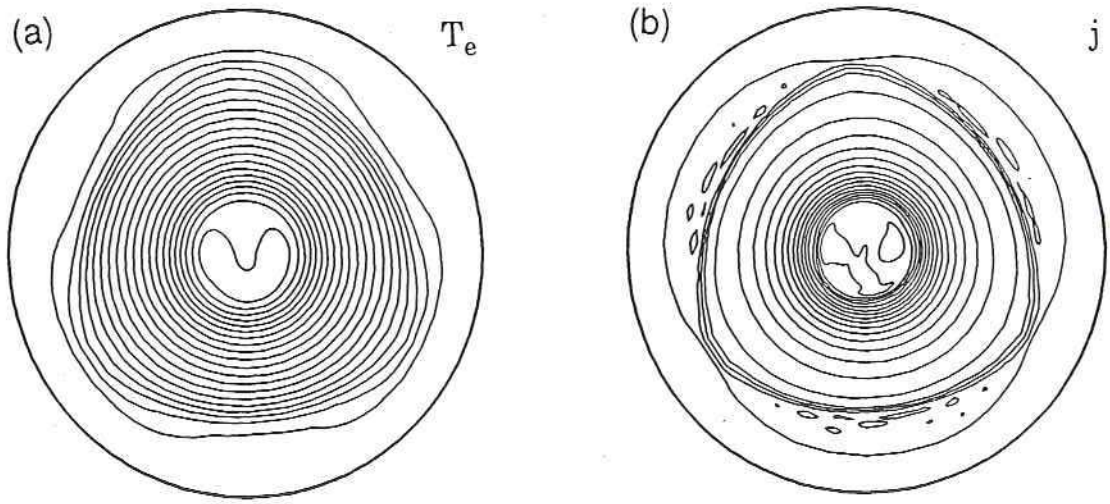

FIGURE 4 Contour plots of (a) electron temperature and (b) current density at the time of maximum 3/1 amplitude during profile contraction.

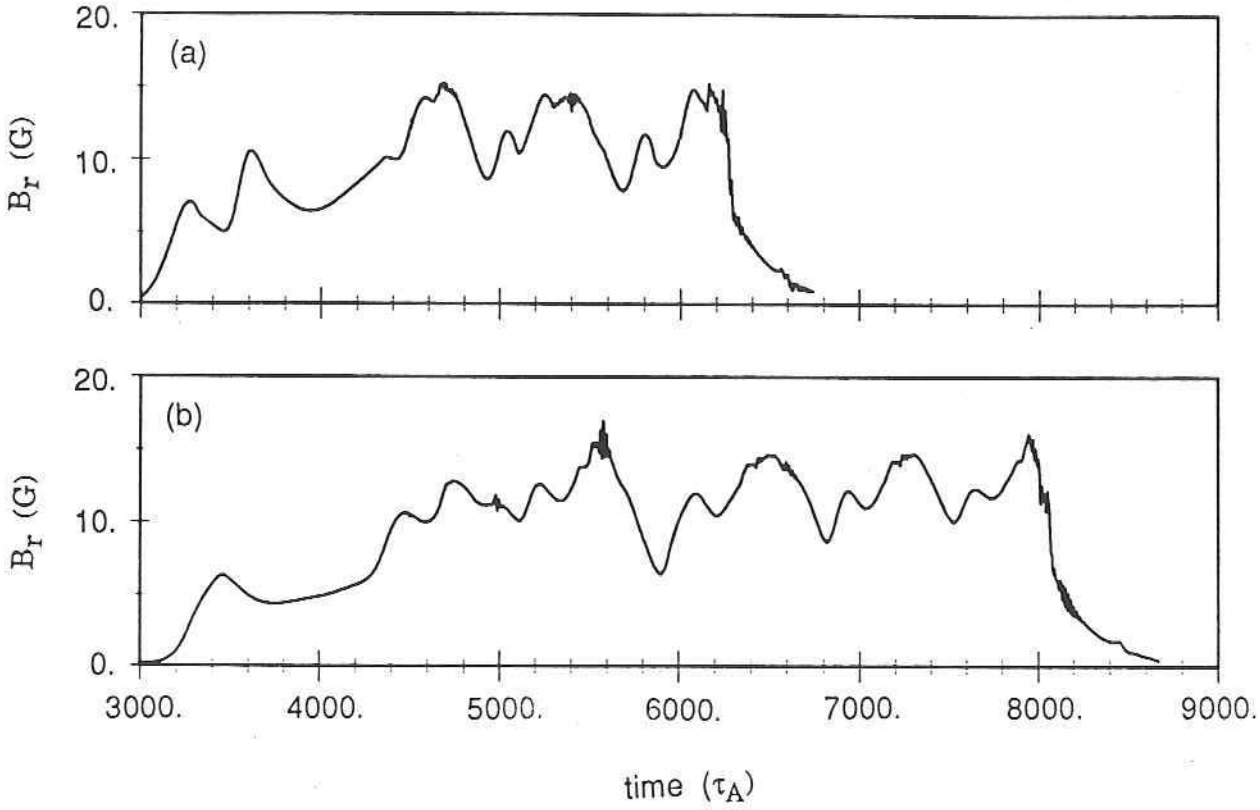

FIGURE 5 Time histories for the 2/1 component of the radial magnetic field at the wall for two runs with E = 2000: (a) with resistivity perturbations and (b) without resistivity perturbations.

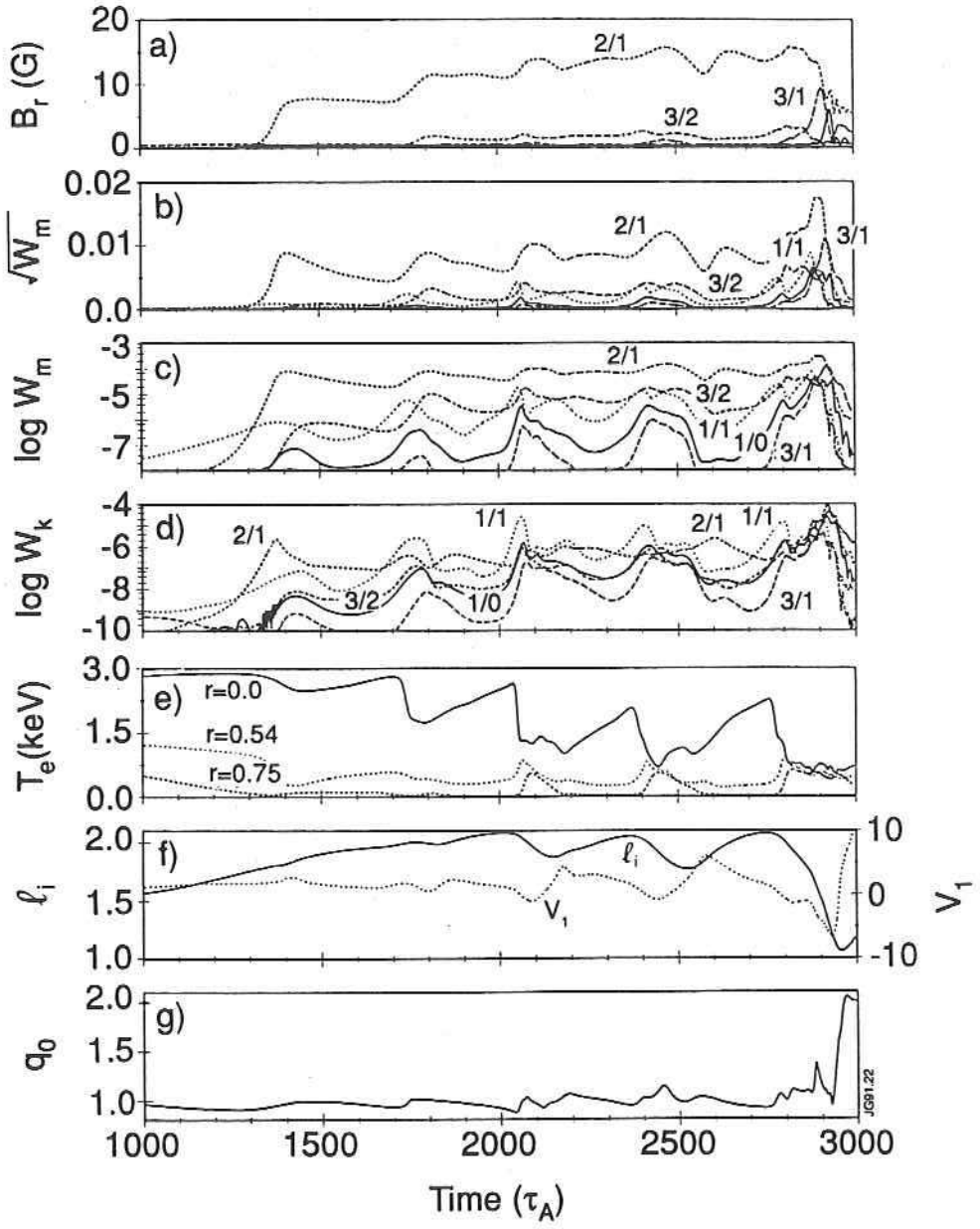

FIGURE 6 Time history of run with E = 5000 discussed in Secs. 4 - 5. (a) Radial magnetic field B_r at the wall, (b) square-root of magnetic energy W_M, (c) logarithm of magnetic energy W_M, (d) logarithm of kinetic energy W_K of the principal modes; (e) electron temperature at the centre, r = 0.54 m, and r = 0.75 m, (f) internal inductance ℓ_i and loop voltage V_ℓ and (g) central safety factor q_0.

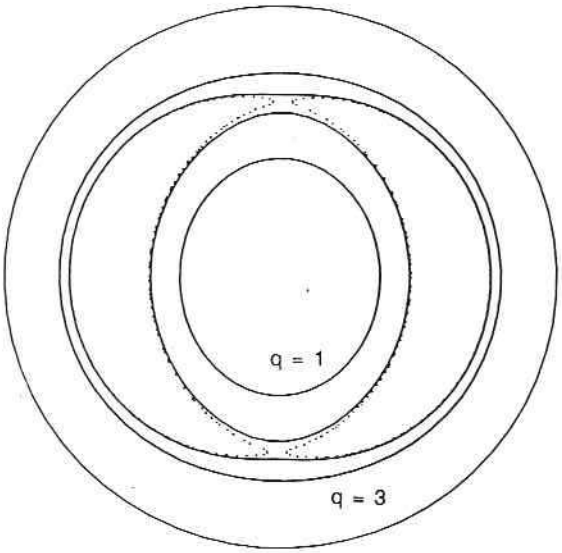

FIGURE 7 Helical q = 2 quasi-equilibrium at the start of a minor disruption, $t/\tau_A = 2383$. The solid lines show the location of q = 1, 3/2, 5/2 and 3, and the dots show the q = 2 separatrix.

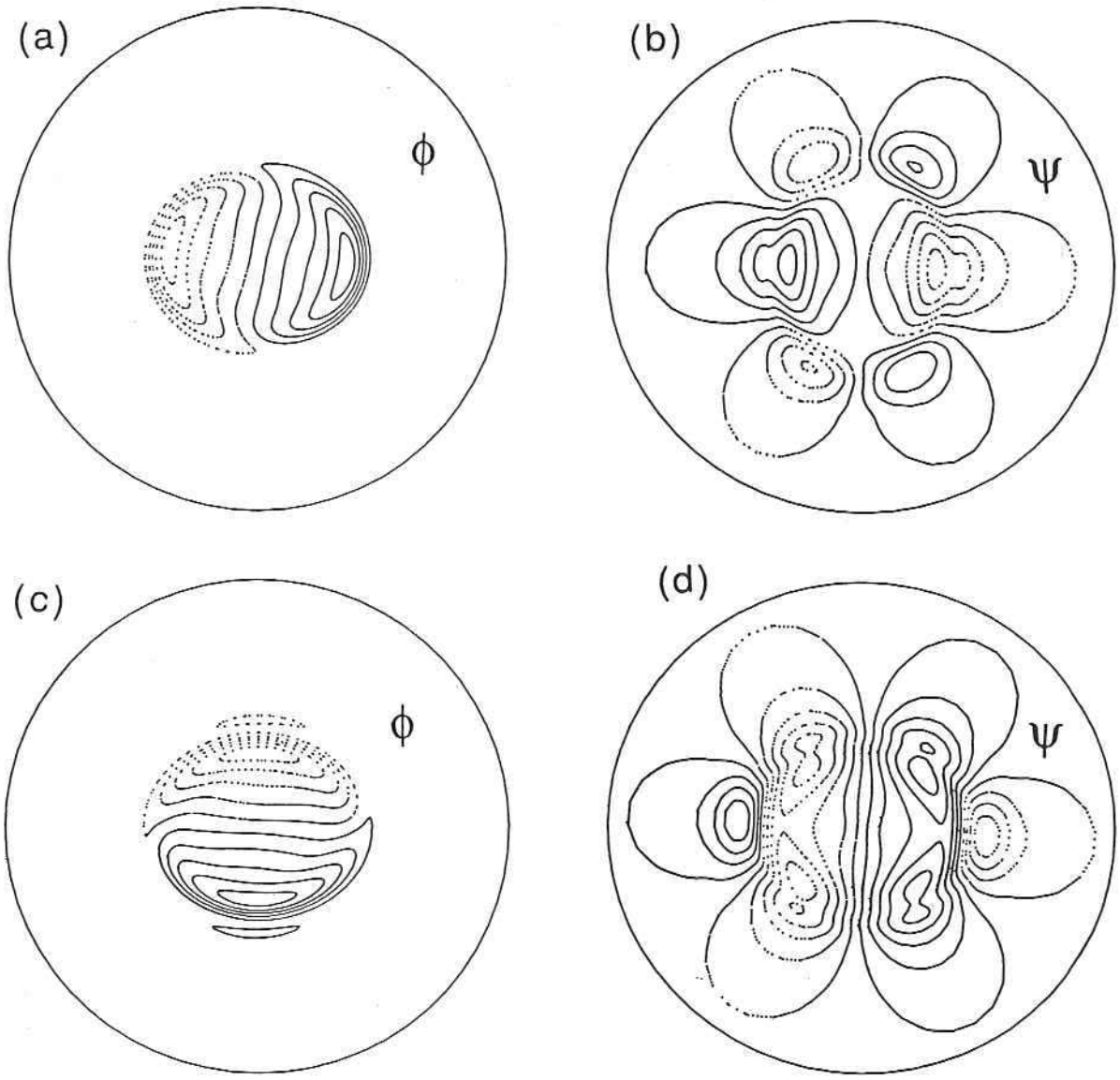

FIGURE 8 Contour plots of ϕ and ψ for unstable eigenmode on the q = 2 helical equilibrium in Fig. 7. (a) shows ϕ and (b) ψ in the same toroidal plane as the equilibrium. (c) shows ϕ and (d) ψ in the opposite toroidal plane (180 degrees apart).

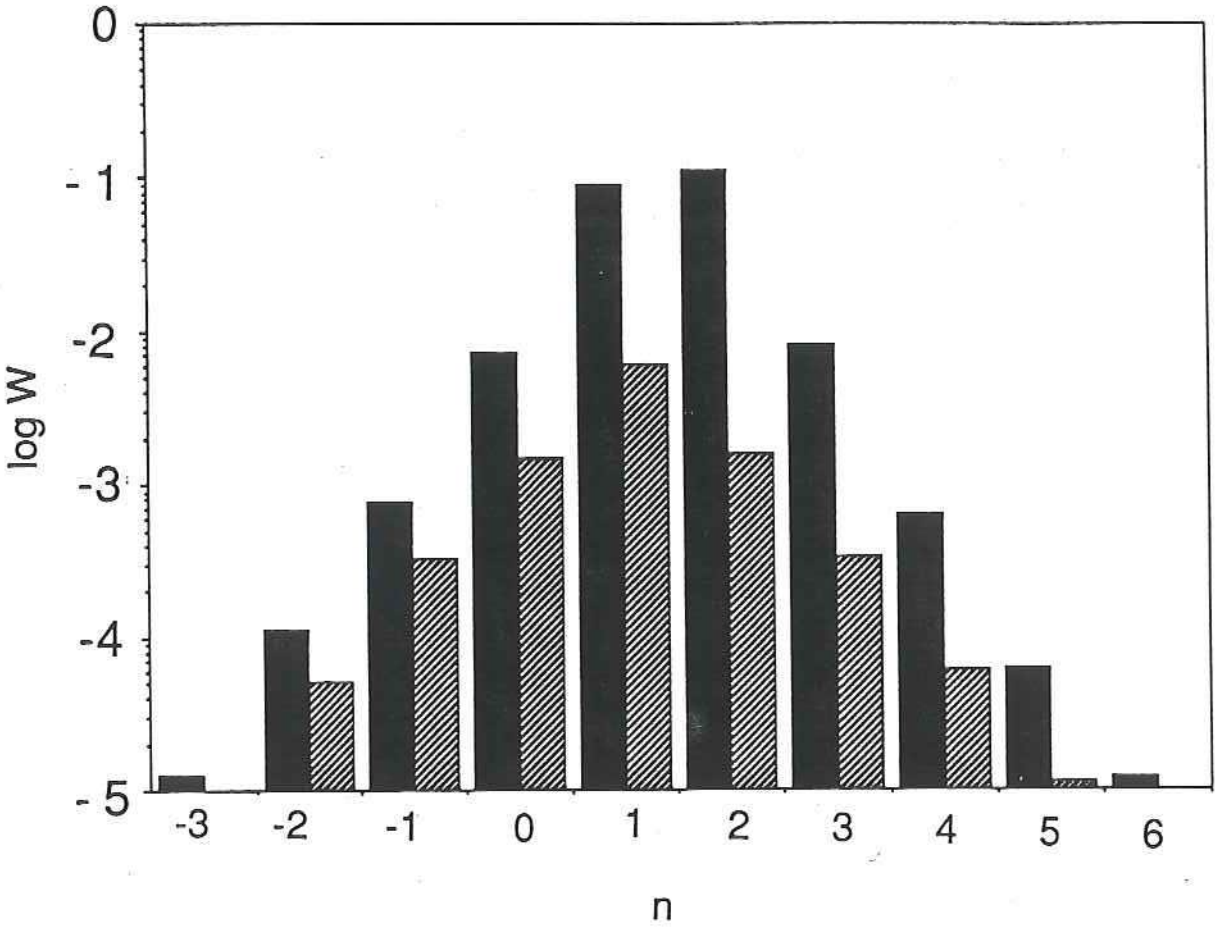

FIGURE 9 Distribution of magnetic (black) and kinetic (hashed) energies in the linear eigenmode with m = 2n -1 that is unstable for the equilibrium in Fig. 7. The dominant component is m=1/n=1 in the kinetic energy and m=3/n=2 in the magnetic energy. Note the significant fraction of -1/0 in the kinetic energy.

FIGURE 10 Electron temperature during a minor disruption at times $t/\tau_A = 2363$, 2405, 2435 and 2553. The colors in Figs. 10 and 11 are, in order of increasing numerical values: blue, green, yellow and red.

FIGURE 11 Current density during a minor disruption at times $t/\tau_A = 2363$, 2405, 2435 and 2553.

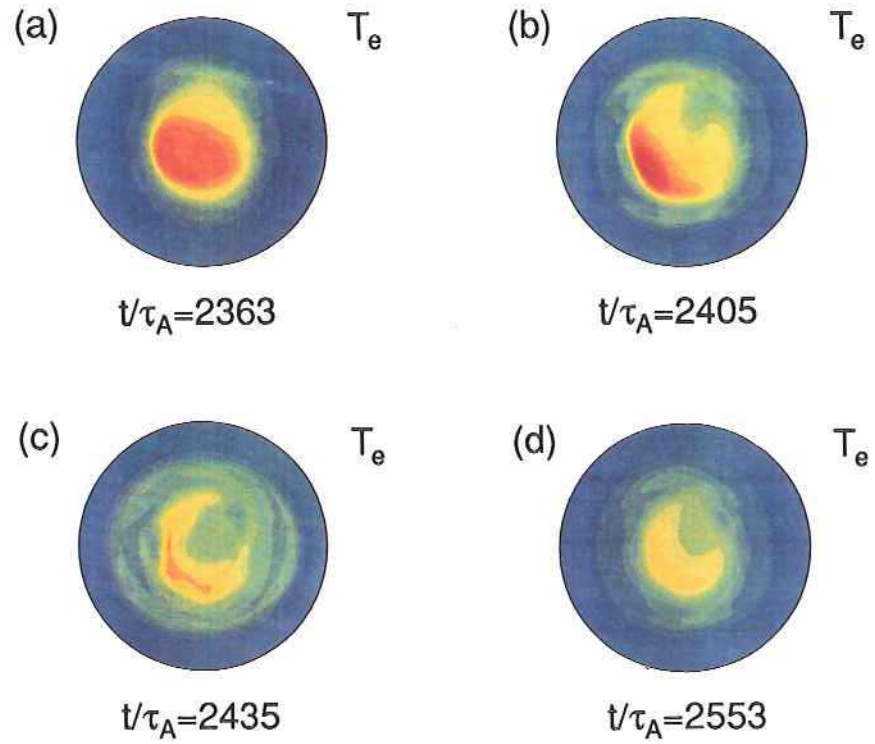
(a)
T_e
(b)
T_e
t/τ_A=2363
t/τ_A=2405
(c)
T_e
(d)
T_e
t/τ_A=2435
t/τ_A=2553

Fig.10

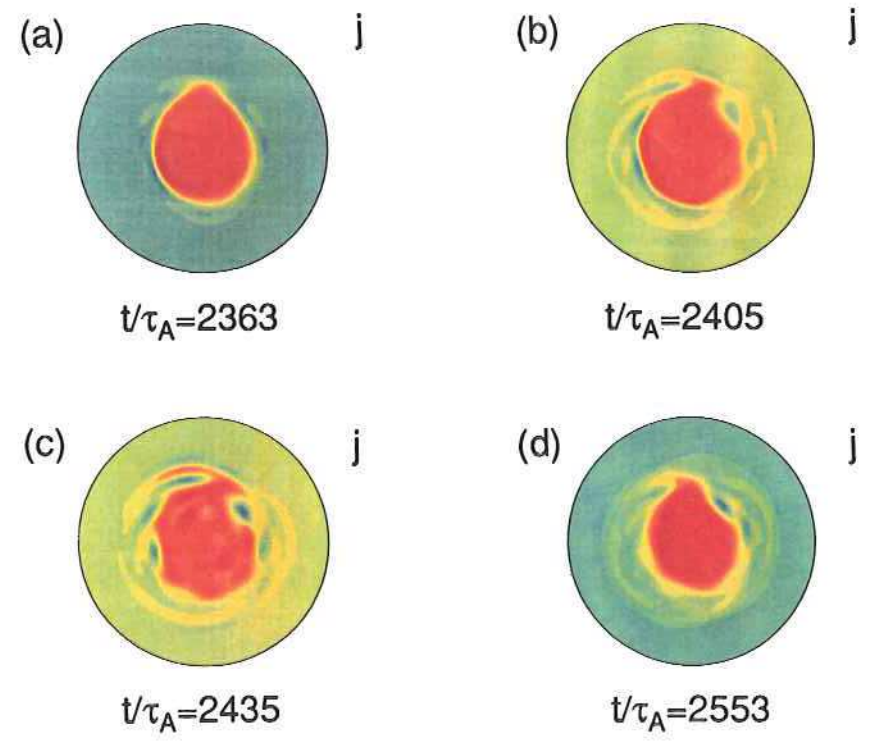
(a)
j
(b)
j
t/τ_A=2363
t/τ_A=2405
(c)
j
(d)
j
t/τ_A=2435
t/τ_A=2553

Fig.11

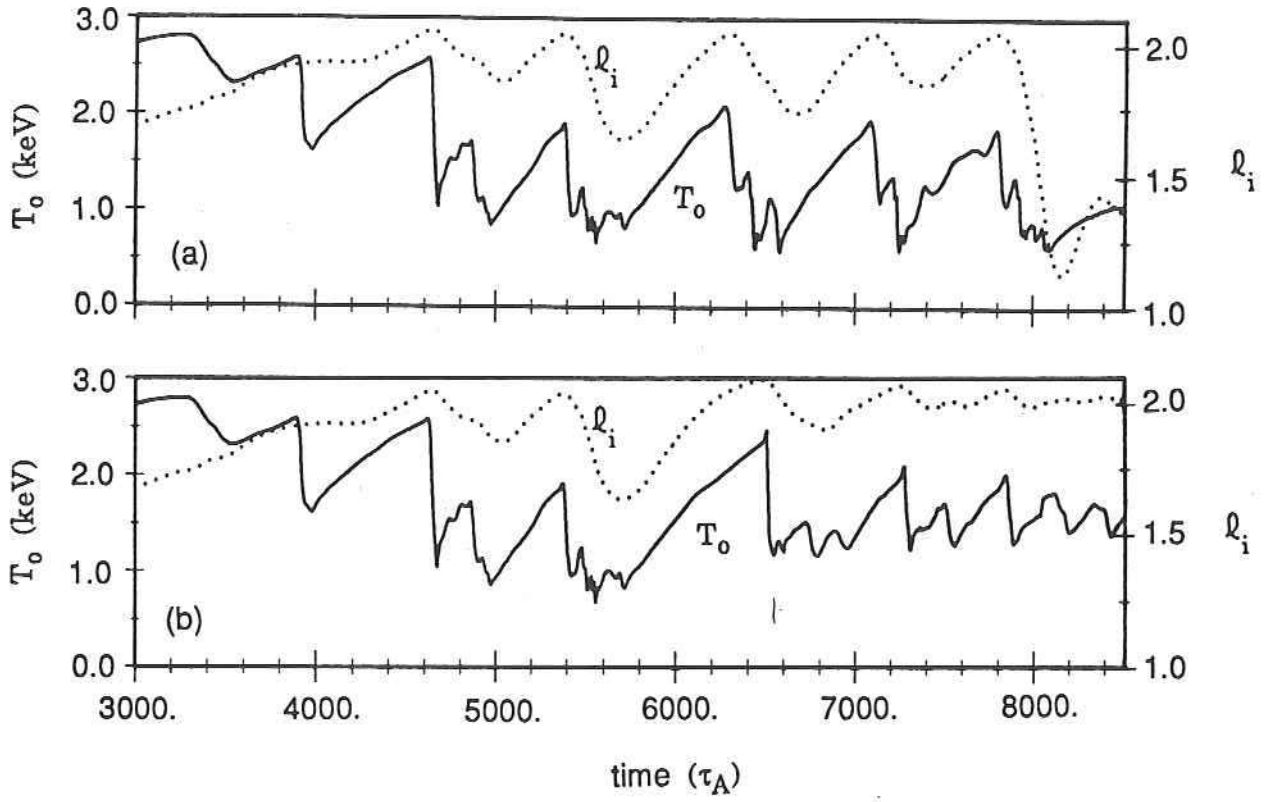

FIGURE 12 Time histories of central electron temperature and internal inductance for two runs with E = 2000. The two runs differ only in that the m=1/n=0 mode was removed from (b) at time $t/\tau_A = 5847$. Note the much reduced amplitude of the minor disruptions and the absence of major disruption in (b).

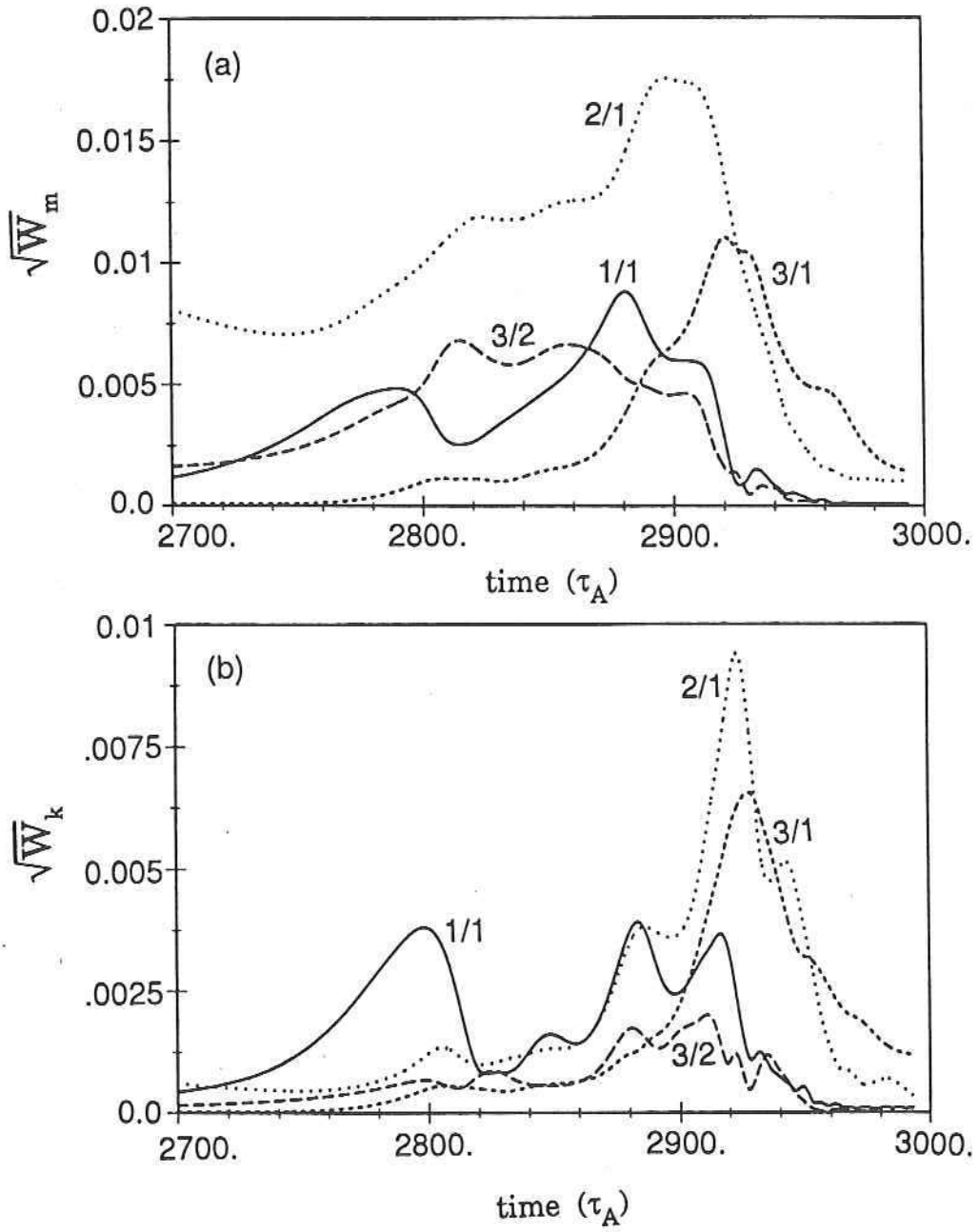

FIGURE 13 Time history of magnetic and kinetic perturbation amplitudes (a) $W_M^{1/2}$ and (b) $W_K^{1/2}$ for the principal modes, during major disruption.

FIGURE 14 (a) Electron temperature T_e, (b) current density j and (c) stream function ϕ together with stream lines, at time $t/\tau_A = 2764$ during internal relaxation leading to major disruption. The colors in the temperature and current plots in Figs. 14 - 18 are, in order of increasing numerical values: blue, green, yellow and red. For the stream function plots, the direction of circulation is clockwise around a red spot.

FIGURE 15 (a) Electron temperature T_e, (b) current density j, and (c) stream function ϕ at time $t/\tau_A = 2795$ at the end of internal relaxation and beginning of current filamentation.

FIGURE 16 (a) Electron temperature T_e, (b) current density j, and (c) stream function ϕ at time $t/\tau_A = 2871$ during current filamentation before rapid growth of m=2/n=1 mode.

FIGURE 17 (a) Electron temperature T_e, (b) current density j, and (c) stream function ϕ at time $t/\tau_A = 2901$ during current broadening at maximum m=2/n=1 amplitude.

FIGURE 18 (a) Electron temperature T_e, (b) current density j, and (c) stream function ϕ at time $t/\tau_A = 2923$ during final phase at maximum m=3/n=1 amplitude.

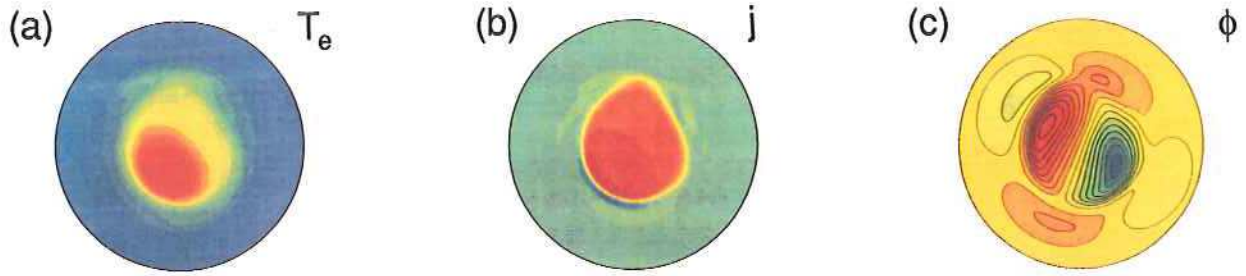

Fig.14 t/τ_A=2764

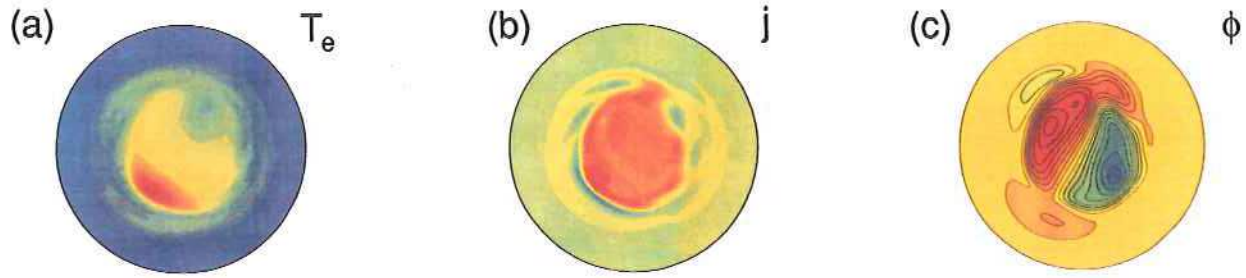

Fig.15 t/τ_A=2795

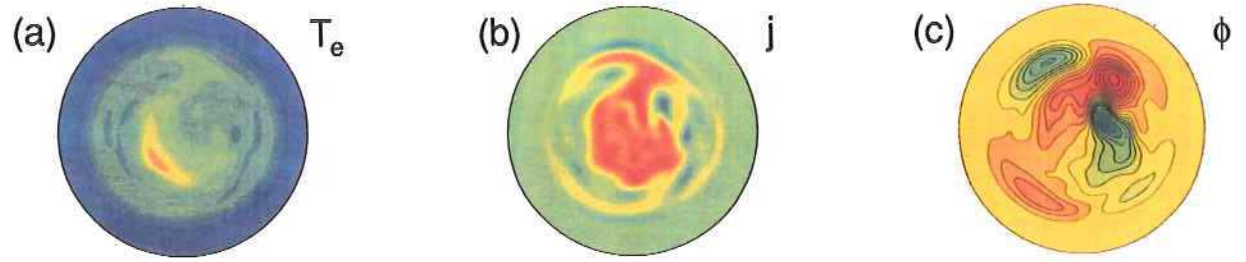

Fig.16 t/τ_A=2871

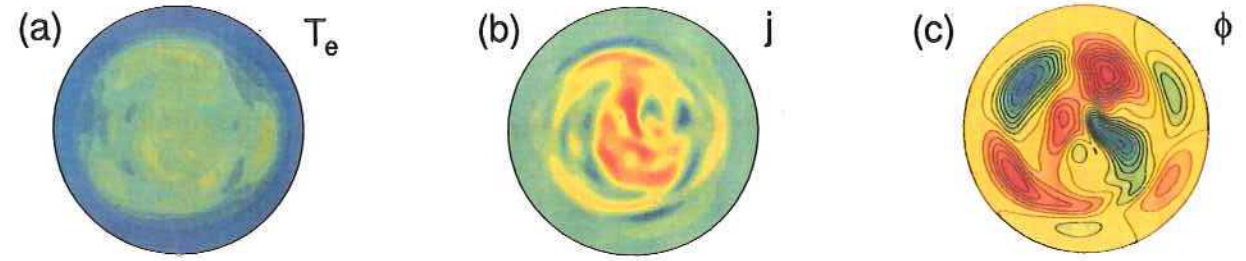

Fig.17 t/τ_A=2901

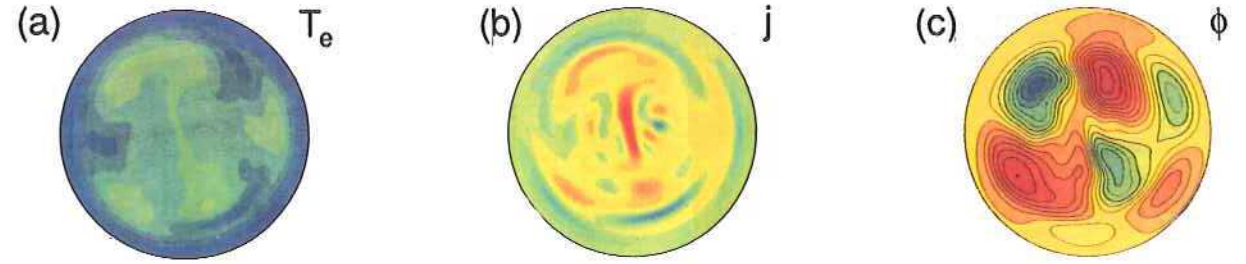

Fig.18 t/τ_A=2923

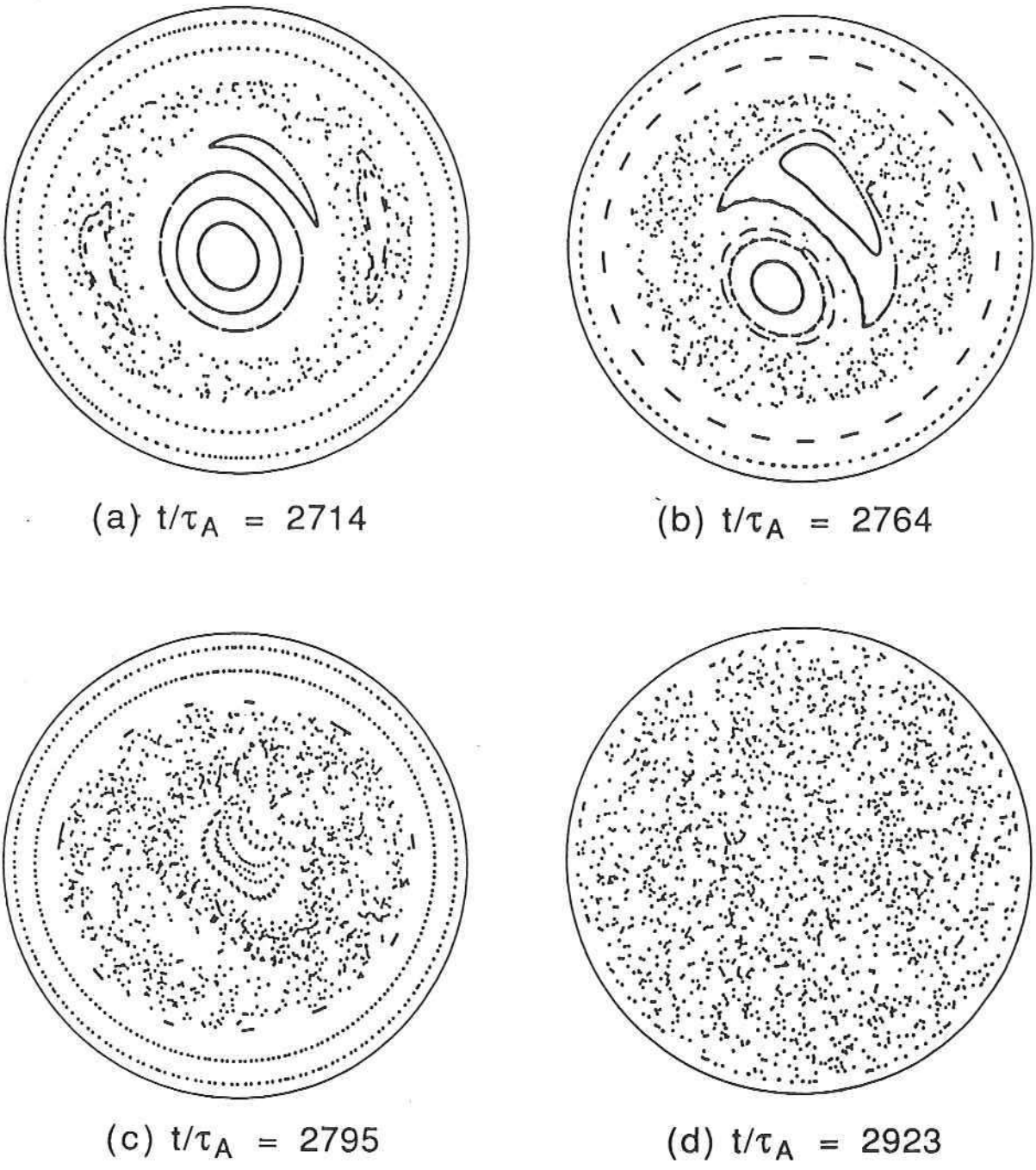

FIGURE 19 Poincaré plots of magnetic field lines in the same toroidal plane as Figs. 14 - 18 at different times during the major disruption. (a) $t/\tau_A = 2714$ (first stage of internal relaxation) (b) $t/\tau_A = 2764$ (during internal relaxation, cf Fig. 14) (c) $t/\tau_A = 2795$ (at the end of internal relaxation, cf Fig. 15) and (d) $t/\tau_A = 2923$ (during final phase at maximum m=3/n=1 amplitude, cf Fig. 18).

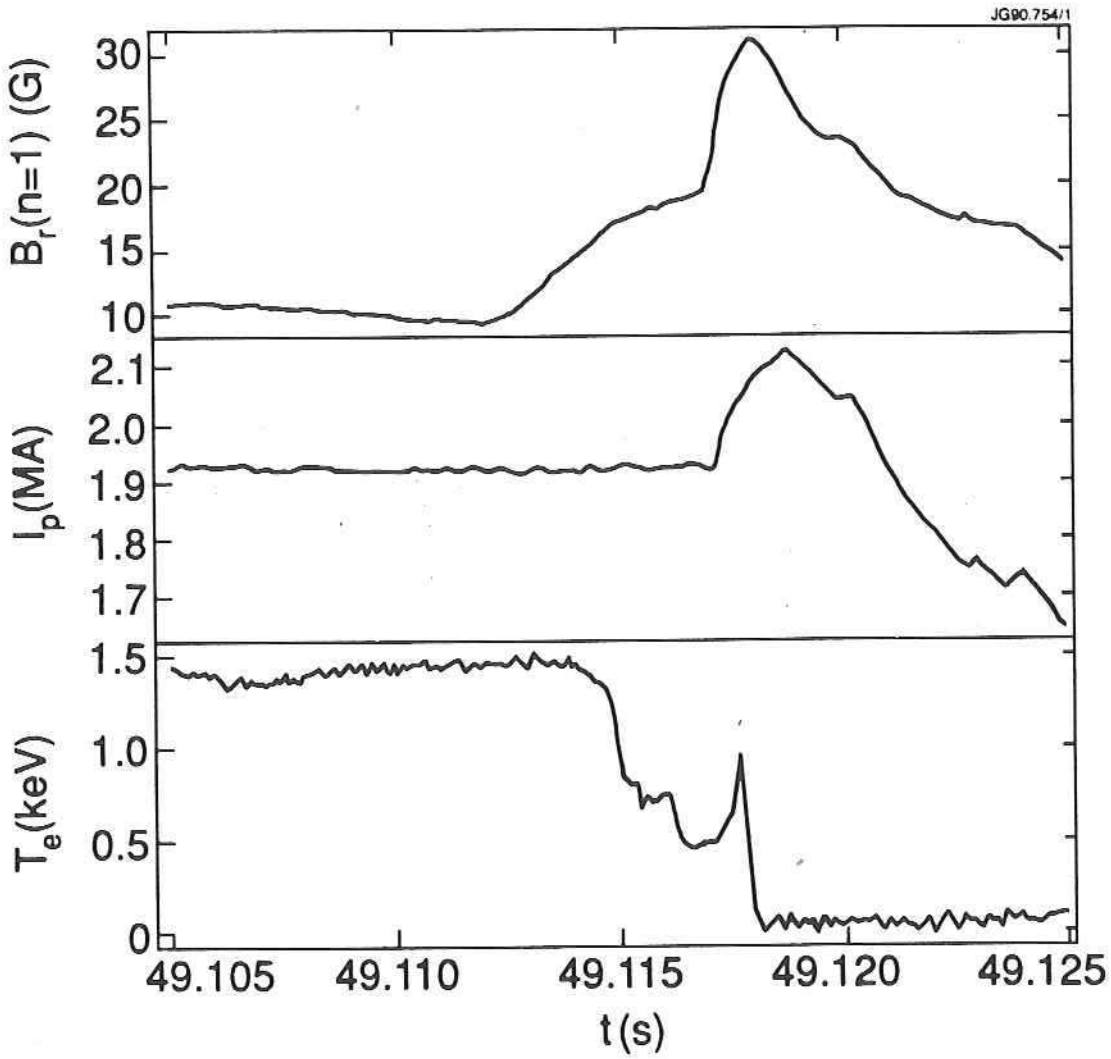

FIGURE 20 Experimental results from a major disruption in JET (shot 11050): (a) n = 1 component of radial magnetic field at the wall, (b) plasma current and (c) electron temperature.

APPENDIX 1.

THE JET TEAM

JET Joint Undertaking, Abingdon, Oxon, OX14 3EA, U.K.

J.M.Adams[1], F.Alladio[4], H.Altmann, R.J.Anderson, G.Appruzzese, W.Bailey, B.Balet, D.V.Bartlett, L.R.Baylor[24], K.Behringer, A.C.Bell, P.Bertoldi, E.Bertolini, V.Bhatnagar, R.J.Bickerton, A.Boileau[3], T.Bonicelli, S.J.Booth, G.Bosia, M.Botman, D.Boyd[31], H.Brelen, H.Brinkschulte, M.Brusati, T.Budd, M.Bures, T.Businaro[4], H.Buttgereit, D.Cacaut, C.Caldwell-Nichols, D.J.Campbell, P.Card, J.Carwardine, G.Celentano, P.Chabert[27], C.D.Challis, A.Cheetham, J.Christiansen, C.Christodoulopoulos, P.Chuilon, R.Claesen, S.Clement[30], J.P.Coad, P.Colestock[6], S.Conroy[13], M.Cooke, S.Cooper, J.G.Cordey, W.Core, S.Corti, A.E.Costley, G.Cottrell, M.Cox[7], P.Cripwell[13], F.Crisanti[4], D.Cross, H.de Blank[16], J.de Haas[16], L.de Kock, E.Deksnis, G.B.Denne, G.Deschamps, G.Devillars, K.J.Dietz, J.Dobbing, S.E.Dorling, P.G.Doyle, D.F.Düchs, H.Duquenoy, A.Edwards, J.Ehrenberg[14], T.Elevant[12], W.Engelhardt, S.K.Erents[7], L.G.Eriksonn[5], M.Evrard[2], H.Falter, D.Flory, M.Forrest[7], C.Froger, K.Fullard, M.Gadeberg[11], A.Galetsas, R.Galvao[8], A.Gibson, R.D.Gill, A.Gondhalekar, C.Gordon, G.Gorini, C.Gormezano, N.A.Gottardi, C.Gowers, B.J.Green, F.S.Griph, M.Gryzinski[26], R.Haange, G.Hammett[6], W.Han[9], C.J.Hancock, P.J.Harbour, N.C.Hawkes[7], P.Haynes[7], T.Hellsten, J.L.Hemmerich, R.Hemsworth, R.F.Herzog, K.Hirsch[14], J.Hoekzema, W.A.Houlberg[24], J.How, M.Huart, A.Hubbard, T.P.Hughes[32], M.Hugon, M.Huguet, J.Jacquinot, O.N.Jarvis, T.C.Jernigan[24], E.Joffrin, E.M.Jones, L.P.D.F.Jones, T.T.C.Jones, J.Källne, A.Kaye, B.E.Keen, M.Keilhacker, G.J.Kelly, A.Khare[15], S.Knowlton, A.Konstantellos, M.Kovanen[21], P.Kupschus, P.Lallia, J.R.Last, L.Lauro-Taroni, M.Laux[33], K.Lawson[7], E.Lazzaro, M.Lennholm, X.Litaudon, P.Lomas, M.Lorentz-Gottardi[2], C.Lowry, G.Magyar, D.Maisonnier, M.Malacarne, V.Marchese, P.Massmann, L.McCarthy[28], G.McCracken[7], P.Mendonca, P.Meriguet, P.Micozzi[4], S.F.Mills, P.Millward, S.L.Milora[24], A.Moissonnier, P.L.Mondino, D.Moreau[17], P.Morgan, H.Morsi[14], G.Murphy, M.F.Nave, M.Newman, L.Nickesson, P.Nielsen, P.Noll, W.Obert, D.O'Brien, J.O'Rourke, M.G.Pacco-Düchs, M.Pain, S.Papastergiou, D.Pasini[20], M.Paume[27], N.Peacock[7], D.Pearson[13], F.Pegoraro, M.Pick, S.Pitcher[7], J.Plancoulaine, J-P.Poffé, F.Porcelli, R.Prentice, T.Raimondi, J.Ramette[17], J.M.Rax[27], C.Raymond, P-H.Rebut, J.Removille, F.Rimini, D.Robinson[7], A.Rolfe, R.T.Ross, L.Rossi, G.Rupprecht[14], R.Rushton, P.Rutter, H.C.Sack, G.Sadler, N.Salmon[13], H.Salzmann[14], A.Santagiustina, D.Schissel[25], P.H.Schild, M.Schmid, G.Schmidt[6], R.L.Shaw, A.Sibley, R.Simonini, J.Sips[16], P.Smeulders, J.Snipes, S.Sommers, L.Sonnerup, K.Sonnenberg, M.Stamp, P.Stangeby[19], D.Start, C.A.Steed, D.Stork, P.E.Stott, T.E.Stringer, D.Stubberfield, T.Sugie[18], D.Summers, H.Summers[20], J.Taboda-Duarte[22], J.Tagle[30], H.Tamnen, A.Tanga, A.Taroni, C.Tebaldi[23], A.Tesini, P.R.Thomas, E.Thompson, K.Thomsen[11], P.Trevalion, M.Tschudin, B.Tubbing, K.Uchino[29], E.Usselmann, H.van der Beken, M.von Hellermann, T.Wade, C.Walker, B.A.Wallander, M.Walravens, K.Walter, D.Ward, M.L.Watkins, J.Wesson, D.H.Wheeler, J.Wilks, U.Willen[12], D.Wilson, T.Winkel, C.Woodward, M.Wykes, I.D.Young, L.Zannelli, M.Zarnstorff[6], D.Zasche[14], J.W.Zwart.

PERMANENT ADDRESS

1. UKAEA, Harwell, Oxon. UK.
2. EUR-EB Association, LPP-ERM/KMS, B-1040 Brussels, Belgium.
3. Institute National des Récherches Scientifique, Quebec, Canada.
4. ENEA-CENTRO Di Frascati, I-00044 Frascati, Roma, Italy.
5. Chalmers University of Technology, Göteborg, Sweden.
6. Princeton Plasma Physics Laboratory, New Jersey, USA.
7. UKAEA Culham Laboratory, Abingdon, Oxon. UK.
8. Plasma Physics Laboratory, Space Research Institute, Sao José dos Campos, Brazil.
9. Institute of Mathematics, University of Oxford, UK.
10. CRPP/EPFL, 21 Avenue des Bains, CH-1007 Lausanne, Switzerland.
11. Risø National Laboratory, DK-4000 Roskilde, Denmark.
12. Swedish Energy Research Commission, S-10072 Stockholm, Sweden.
13. Imperial College of Science and Technology, University of London, UK.
14. Max Planck Institut für Plasmaphysik, D-8046 Garching bei München, FRG.
15. Institute for Plasma Research, Gandhinagar Bhat Gujat, India.
16. FOM Instituut voor Plasmafysica, 3430 Be Nieuwegein, The Netherlands.
17. Commissiariat à L'Energie Atomique, F-92260 Fontenay-aux-Roses, France.
18. JAERI, Tokai Research Establishment, Tokai-Mura, Naka-Gun, Japan.
19. Institute for Aerospace Studies, University of Toronto, Downsview, Ontario, Canada.
20. University of Strathclyde, Glasgow, G4 ONG, U.K.
21. Nuclear Engineering Laboratory, Lapeenranta University, Finland.
22. JNICT, Lisboa, Portugal.
23. Department of Mathematics, Univeristy of Bologna, Italy.
24. Oak Ridge National Laboratory, Oak Ridge, Tenn., USA.
25. G.A. Technologies, San Diego, California, USA.
26. Institute for Nuclear Studies, Swierk, Poland.
27. Commissiariat à l'Energie Atomique, Cadarache, France.
28. School of Physical Sciences, Flinders University of South Australia, South Australia SO42.
29. Kyushi University, Kasagu Fukuoka, Japan.
30. Centro de Investigaciones Energeticas Medioambientales y Techalogicas, Spain.
31. University of Maryland, College Park, Maryland, USA.
32. University of Essex, Colchester, UK.
33. Akademie de Wissenschaften, Berlin, DDR.

CR 88.49.1A